Investigation of Explicit Filtering Strategies for the Lattice Boltzmann Method

Rayane Ait Oubahou

Master of Engineering

Department of Mechanical Engineering

McGill University

Montreal,Quebec

August 27, 2020

A thesis submitted to McGill University in partial fulfillment of the requirements of the degree of Master of Engineering

Contents

List of Figures

List of Tables

Abstract

Different explicit filtering strategies for the Lattice Boltzmann Method (LBM) were implemented and analyzed using the open source solver *Palabos* and the solver *Mathematica*. A von Neumann analysis performed by Ricot *et al.* showed that instabilities occuring for the the single relaxation time (BGK) formulation of the LBM are caused by the interaction of acoustic modes with other modes in the simulations. Moreover, the BGK-VLES (very large eddy simulation) formulation, which uses a turbulence model, causes high numerical dissipation in the flow field solution. One alternative called the LBM- Multi-Relaxation Times (LBM-MRT) is to perform collision on moments of the distribution function. This approach leads to a more stable and physical formulation, but the LBM-MRT tends to increase computational costs. In the present study, an explicit filter (*i.e.* SF-7) was first implemented with the multi-relaxation times (MRT) formulation of the LBM. A Dual Shear Layer benchmark case was implemented and results compared with the unfiltered BGK and MRT, and filtered BGK for four grid sizes. It was shown that explicitely filtering the MRT leads to enhanced stability in comparision with the unfiltered MRT, with the filtered scheme successfully preventing spurious vortices for under-resolved simulations. A three-dimensional Taylor-Green Vortex test case was also investigated. In three-dimensions, the filtered scheme was shown to accurately capture the isotropic turbulence decay while significantly decreasing oscillations in the solution. The Von Neumann analysis of a differential filter, based on the Approximate Deconvolution Model (ADM) techniques, was performed in conjunction with that of the BGK without an additional turbulence model. The differential filter was shown to increase the dissipation of some modes in the solution. While this demonstrates the possible application of an approximate deconvolution-based filter on the LBM, further optimization of the filter parameters is necessary in order to stabilize the scheme.

Résumé

Dans la présente thèse, différentes stratégies de filtrage explicites pour la méthode de Boltzmann sur Réseau (LBM) ont été implementées et analysées à l'aide des solveurs Palabos et Mathematica. Une analyse de Von Neumann réalisée par Ricot et al. a montré que les instabilités visibles pour la formulation de temps de relaxation unique (BGK) de LBM sont causées par l'interaction des modes acoustiques avec d'autres modes dans les simulations. De plus, la formulation BGK-VLES (simulations des très grandes structures de turbulence), qui utilise un modèle de turbulence, conduit à une dissipation élevée dans la solution de champ d'écoulement. Une alternative consiste à effectuer le processus de collision sur les moments de la fonction de distribution, ce qui mène à une formulation plus stable et réaliste, la formulation aux temps de relaxation multiples (LBM-MRT). Cependant, cela entraîne également des coûts de calcul plus élevés. Un filtre explicite (SF-7) fut d'abord implementé avec la formulation à temps de relaxation multiples (MRT) de la méthode de Boltzmann sur réseau. Un cas de référence de double couche de cisaillement a d'abord été réalisé et les résultats comparés avec les versions filtrées et non filtrées des formulations BGK et MRT pour quatre tailles de maillage. Il a été démontré que le filtrage explicite du MRT conduit à une stabilité accrue par rapport au MRT non filtré, le schéma filtré empêchant avec succès les tourbillons parasites pour les simulations sous-résolues. Une simulation tri-dimensionelle de Taylor-Green Vortex a également été réalisée. En trois dimensions, le schéma filtré a pu capturer avec précision la décroissance de la turbulence isotrope tout en diminuant considérablement les oscillations dans la solution. L'analyse de Von Neumann d'un filtre différentiel, basée sur les techniques du modèle de déconvolution approximative (ADM), a été menée conjointement avec le BGK sans modèle de turbulence supplémentaire. Il a été démontré que le filtre différentiel augmente la dissipation de certains modes dans la solution. Bien que cela

démontre l'application possible d'un filtre basé sur la déconvolution approximative sur le LBM, une optimisation supplémentaire des paramètres du filtre est nécessaire.

Acknowledgements

I would like to give my thanks and express my love to my brother, Wassim Ait Oubahou, my mother, Fatima El Hilali, and my father, Ahmed Ait Oubahou, for their constant love, support, and advice. I would not be here without them today.

I would like to express my infinite gratitude to my supervisor Professor Luc Mongeau. The books, resources, time, advice and financial support he has provided have made this thesis possible.

I would like to thank my collegue Mostafa Najafi-Yazdi for the time he has taken to give me advice and our discussions.

My next thanks go out to my collegues Song Wang and Miguel Chavez-Modena, for their precious discussions and for time spent helping me with *Palabos*.

Finally, I would like to thank the rest of my family, friends, and collegues who have been here throughout the years and provided love and support in any way. I am grateful for you.

Contributions

The contributions of this thesis are as follows:

- Implementation of an explicit filter on the MRT collision operator (Chapter 6).
- Conduction of a Von Neumann analysis on the LBM-MRT with the SF-7 explicit filter and quantification of the dispersive and dissipative properties of the D2Q9 (Chapter 5).
- Conduction of a Von Neumann analysis on the LBM-BGK with an ADM-based filter and quantification of the dispersive and dissipative properties of the D2Q9 (Chapter 5).
- Benchmarking of the explicit filtering approach with a two-dimensional dual shear layer and a three-dimensional Taylor Green Vortex case (Chapter 6).

Chapter 1

Introduction

In this study, new strategies for the stabilization of the LBM were investigated, and verified through simulations of benchmark test cases. In particular, explicit filtering strategies were studied. For the first time, an explicit filter was implemented with the Multi-relaxation time (MRT) scheme of the Lattice Boltzmann Method (LBM). Then, a second filter based on the approximate deconvolution model (ADM) was implemented. In both cases, a von Neumann Analysis was conducted and both the dispersive and dissipative properties of the scheme qualified. Two benchmark tests was conducted: 1) a two-dimensional dual shear layer case; and 2) a three-dimensional Taylor-Green vortex case. The thesis is organized as follows. In the first part, governing equations of Computational Fluid Dynamics (CFD) are presented as well as existing solution methods and turbulence models. Then, the kinetic theory is presented and the link between the Lattice Gas Automata (LGA) and the LBM explained and defined.

1.1 Computational Fluid Dynamics

1.1.1 Navier-Stoke Equations

The Navier-Stokes equations describe the behavior of a fluid and are derived from the principles of mass, momentum, and energy conservation. They are expressed as

$$\frac{\partial \rho}{\partial t} + \frac{\partial \rho u_i}{\partial x_j} = 0, \tag{1.1}$$

and

$$\frac{\partial \rho u_i}{\partial t} + u_j \frac{\partial \rho u_i}{\partial x_j} = -\frac{\partial p}{\partial x_i} + \frac{\partial \tau_{ij}}{\partial x_j}, \tag{1.2}$$

with τ_{ij} the tensor of viscous forces defined as

$$\tau_{ij} = 2\mu S_{ij} + \left(\mu_B - \frac{2}{3}\mu\right) S_{kk}\delta_{ij}. \tag{1.3}$$

The strain rate tensor, S_{ij}, is defined as:

$$S_{ij} = \frac{1}{2}\left(\frac{\partial u_i}{\partial x_j} + \frac{\partial u_j}{\partial x_i}\right), \tag{1.4}$$

and μ_B the bulk viscosity. Usually, Stoke's hypothesis is used and the second term of τ_{ij} expressed as $\left(-\frac{2}{3}\mu\right) S_{kk}\delta_{ij}$.

Finally, the equation of conservation of energy is expressed as

$$\frac{\partial \rho e}{\partial t} + \frac{\partial \rho e u_i}{\partial x_i} = -\frac{\partial q_i}{\partial x_i} - p\frac{\partial u_i}{\partial x_i} + \tau_{ij}\frac{\partial u_i}{\partial x_j}. \tag{1.5}$$

Under some assumptions which simplify them, the Navier-Stokes equation can admit analytical solutions, but in most practical situations require numerical methods to solve them.

1.1.2 Turbulence Modeling

Real flows are often turbulent and are characterized by a three-dimensional behavior, high vorticity, and are due to a very high kinetic energy present in the flows. The kinetic energy is transferred from the large scales to the smallest scales via what is known as the energy cascade, introduced by Kolmogorov [1]. These smallest scales then dissipate the kinetic energy with heat production as a by product. This vast range of scales often precludes direct computation without simplifications, usually through the modeling of the smallest scales. It is customary in the field to argue that the smallest scales are universal, and so

their effect on the largest scales can be modeled. It was Boussinesq [2, 3] who first introduced the concept of turbulent viscosity, also known as eddy viscosity. He modeled the effect of turbulent stresses on the mean flow as a modified viscosity. Boundaries conditions were then considered into subsequent models such as the mixing length model by Prandtl [4], algebraic models [5], one equation models, and two equation models [6]. In Direct Numerical Simulation(s) (DNS), all scales in the fluid are directly computed without modeling of the small scales, with the smallest grid size commensurate the smallest scales in the flow. While the method is accurate, it also requires very fine grids especially in regions of high gradients or boundary layers. In more complex cases, involving multiphases or highly turbulent flows, the computational cost of such simulations is too high and so, alternatives must be sought. The Reynolds-averaged Navier-Stokes (RANS) equations correspond to a time-averaging of the governing equations. The solution is a time averaged profile of the variables. Turbulence models are derived based on either the eddy viscosity or mixing length hypothesis, and some of the most common are the $k-\omega$ [7], $k-\epsilon$ [6], and the Spallart-Allmaras [8, 9]. Each of these models represent different flow cases. While accurate, these models are based on empirical constants which may vary from one application to another. Choosing the correct model for an application is important, as the wrong model can give inaccurate or unrealistic results. First introduced by Smagorinsky to simulate atmospheric currents of air [10], Large Eddy Simulations (LES) are a good compromise between DNS and RANS. In this methodology, a low pass filtering approach is adopted. Larger scales with lower wavenumbers are directly computed while smaller scales are modeled via a turbulent viscosity approach. Two scales are particularly relevant in the LES approach: the domain characteristic length Ł, and the grid size, ∇x. Starting from the Navier-Stokes equations,

$$\frac{\partial u_i}{\partial t} + \frac{\partial u_i u_j}{\partial x_j} = -\frac{1}{\rho}\frac{\partial p}{\partial x_i} + \nu \frac{\partial^2 u_i}{\partial x_j \partial x_j}, \tag{1.6}$$

filtering is applied as (*i.e.* in the following and the rest of the thesis, an overbar will be placed over filtered terms)

$$\frac{\partial \overline{\rho u_i}}{\partial t} + \frac{\partial \overline{u_i u_j}}{\partial x_j} = -\frac{1}{\rho}\frac{\partial \overline{p}}{\partial x_i} + \nu \frac{\partial^2 \overline{u_i}}{\partial x_j \partial x_j}. \tag{1.7}$$

As the unfiltered variables are unknowns, the term $\partial \overline{u_i u_j}$ cannot be directly computed.

As $\partial \bar{u}_i \bar{u}_j$ is known, a substitution is made in the LES framework,

$$\frac{\partial \overline{\rho u_i}}{\partial t} + \frac{\partial \bar{u}_i \bar{u}_j}{\partial x_j} = -\frac{1}{\rho}\frac{\partial \bar{p}}{\partial x_i} + \nu \frac{\partial^2 \overline{u_i}}{\partial x_j \partial x_j} + \left(\frac{\partial \overline{u_i u_j}}{\partial x_j} - \frac{\partial \bar{u}_i \bar{u}_j}{\partial x_j} \right). \tag{1.8}$$

Let $T_{ij} = \overline{u_i u_j} - \bar{u}_i \bar{u}_j$. The filtered Navier-Stokes equation can then be expressed as

$$\frac{\partial \overline{\rho u_i}}{\partial t} + \frac{\partial \bar{u}_i \bar{u}_j}{\partial x_j} = -\frac{1}{\rho}\frac{\partial \bar{p}}{\partial x_i} + \nu \frac{\partial^2 \overline{u_i}}{\partial x_j \partial x_j} + \left(\frac{\partial T_{ij}}{\partial x_j} \right). \tag{1.9}$$

The quantity T_{ij} englobes the Sub-grid Scales stresses and is the resulting extra term. The goal of the LES method is then to model T_{ij}, and different models can be chosen depending on the targeted application. In the Smagorinsky-Lilly SGS model, T_{ij} is defined as

$$T_{ij} = -\mu_{SGS} \left(\frac{\partial \overline{u_i}}{\partial x_j} + \frac{\partial \overline{u_j}}{\partial x_i} \right) + \frac{1}{3} T_{ii} \delta_{ii}. \tag{1.10}$$

In this expression, the viscosity μ_{SGS} which is defined as

$$\mu_{SGS} = \rho C_{SGS} \nabla^2 S = \rho C \nabla^2 2 S_{ij} S_{ij}. \tag{1.11}$$

C is a constant and the filtered strain rate tensor is defined as

$$\overline{S_{ij}} = \frac{1}{2} \left(\frac{\partial \overline{u_i}}{\partial x_j} + \frac{\partial \overline{u_j}}{\partial x_i} \right). \tag{1.12}$$

Two types of LES models exist; in the explicit LES, the filter function is explicitely defined whereas in the implicit LES, the grid is assumed to be the cut-off. Scales smaller than the grid cutoff are not directly computed.

1.1.3 Turbulence Modelling in LBM

Smagorinsky Model

In the Large Eddy Simulations (LES) approach, the effect of turbulent scales can be accounted for via a modification of the viscosity to yield an effective viscosity. In the LBM, a similar approach is adopted. As viscosity is linked to the relaxation time, subgrid scales models can be implemented via a modification of the relaxation time [11, 12, 10],

$$\tau_{eff} = \tau + \tau_{SGS}, \tag{1.13}$$

with τ_{SGS} the relaxation time corresponding to the turbulent eddy-viscosity ν_{SGS}

$$\tau_{SGS} = \nu_{SGS} {c_s}^2 \Delta t. \tag{1.14}$$

The effective viscosity is expressed as

$$\nu_{eff} = \nu + \nu_{SGS}, \tag{1.15}$$

with

$$\nu = {c_s}^2 \tau - 12\Delta t, \tag{1.16}$$

and

$$\nu_{SGS} = c_s \Delta^2 * (|S| - S). \tag{1.17}$$

S is the strain rate tensor defined as

$$S_{ij} = \frac{1}{2}\left(\frac{\partial u_i}{\partial x_j} + \frac{\partial u_j}{\partial x_i}\right). \tag{1.18}$$

This approach is most commonly called "LBM-VLES", where the "VLES" stands for "Very Large Eddy Simulations".

1.2 Lattice Gas Automata (LGA)

The Lattice gas Automata, introduced by Hardy, Pomeau, and de Pazzis in the 1970's, is the precursor to the LBM [13, 14]. In the LGA model, particles are free to move between the sites of a lattice. Each site has a Boolean state. At any moment in time, a particle may or may not be present on the site. Particles move along the links of the lattice while following streaming and collision rules when two particles reach the same state at the same time. While being a simple model, such Boolean description of the fluid flow has some disadvantages. It tends to produce significant statistical noise as each particle needs to be tracked independently. In addition, a large number of particles is necessary to reach a

realistic solution, which increases computational costs. Finally, it lacks Galilean invariance. The Lattice Boltzmann Method circumvents these problems by replacing the Boolean states by a particle distribution function which translates the probability for a group of particles to be moving in a certain direction. The distribution function itself is an averaged quantity, so there is no need to perform further averaging over the cells.

1.3 Lattice Boltzmann Equation (LBE)

The dynamics of particles for an ideal gas can be described via the Boltzmann equation (BE) [15],

$$\frac{\partial f}{\partial t} + \vec{u} \bullet \nabla \mathrm{f} = \Omega. \tag{1.19}$$

In this equation $f(x,t)$ the particle distribution function, $\vec{u}$ the particle velocity, and Ω the collision operator. The Lattice Boltzmann Method simplifies this idea by reducing the number of possible directions, and forcing particles to move on a discrete lattice, yielding the Lattice Boltzmann Equation (LBE) [16] as

$$f_i(\vec{x} + c\vec{e_i}\Delta t, t + \Delta t) = f_i(x,t) - \frac{1}{\tau}[f_i(x,t) - {f_i}^{eq}(x,t)]. \tag{1.20}$$

In this equation, $f_i(\vec{x},t)$ are the initial particle distributions , $f_i(\vec{x} + c\vec{e_i}\Delta t, t + \Delta t)$ are the updated populations, ${f_i}^{eq}(\vec{x},t)$ the equilibrium distribution, and τ is the relaxation time towards equilibrium (*i.e.* the time it takes for particle populations to reach their equilibrium values).

This is usually known as the LBM-Single Relaxation Time (LBM-SRT) or LBM-Bhatnagar-Gross-Krook (LBM-BGK) formulation.

1.4 From the LBE to the Navier-Stokes Equations

It is mandatory to be able to relate the Lattice Boltzmann Equation to the macroscopic equations [17]. In particular, one might want to relate the relaxation time τ to the macroscopic viscosity ν. It can be shown [18] that, at very small scales, characterized by a small

Knudsen number ($i.e\ Kn = \varepsilon \to 0$), $f = f^{eq}$ is solution to the Euler equations. At these scales, the flow behavior is free of viscosity and heat effects and is completely described by the Euler equations. The argument is then that, since the Navier-Stokes equations are similar to the Euler equations, their solution, f, must be close tof^{eq}. A multi-scale expansion can then be introduced; f can then be considered as a small deviation from f^{eq}, with

$$f = f^{eq} + f^{neq}, \tag{1.21}$$

and

$$f = f^0 + \varepsilon f^1 + \varepsilon^2 f^2, \tag{1.22}$$

where $f^0 = f^{eq}$. This translates the fact that different physical phenomena occur at different scales; at microscopic scales when $f = f^{eq}$, the flow is entirely described by the Euler equations whereas at microscopic scales when f deviates from f^{eq}, the Navier-Stokes are needed to account for the effects of viscosity. This procedure is known as the Chapman-Enskog expansion[19]. More details are given in the Appendix.

1.5 Lattice Boltzmann Applications

Due to its simplicity and reduced computational costs, the Lattice Boltzmann Method (LBM) has gathered significant interest for numerical simulations of industrial flows. As a mesoscopic method, the LBM tracks the local motion of groups of particles who can stream to their immediate neighbor cells during each time step. Therefore, the algorithm is considered local and simulations can be easily parallelized, making them fast and efficient. Another advantage lies in the straightforward handling of boundary conditions. There is no need to generate a computational mesh defined by analytical functions. As in the immersed boundary method, surfaces can be represented as solid objects within a uniform isometric grid.

These advantages have led to the use of the LBM in areas as diverse as aeroacoustics [20, 21, 22], aerodynamics [23, 24, 25], porous media flows [26, 27], earth sciences (*i.e.* soil filtration) [28], simple flows [29], mold filling [30], and biomedical flows such as blood flows [31, 32, 33, 34, 35], among others.

In the last decade, the LBM has also gathered growing interest in detailed flow simulations and more specifically aeroacoustic simulations. In such simulations, the ability of the method to handle complex boundaries enables the inclusion of the jet nozzle in the computational domain. Many studies have also implemented the LBM with a Large Eddy Simulations or a Direct Numerical Simulation approach.

In a 2010 report, Lew et al. [20] simulated a subsonic turbulent round jet and predicted the noise field in the far field. In the near-field, parameters such as turbulence and vorticity levels and isosurfaces, and jet velocity decay rate on the jet centerline were gathered. Results were then compared with experimental and Navier-Stokes based LES simulations, and good agreement was observed, with a 2 dB difference in the noise levels. In his thesis, Gong [21] used the LBM-based solver PowerFLOW to simulate the flow through lobed mixers and directly compute the associated radiated sound. Different parameters were studied: the number of lobes, the lobe depth, and the scalloping. In the near field, results such as vorticity isocontours and jet centerline velocity decay rate were obtained. In the far-field, acoustic levels (*i.e.* Overall Sound Pressure Level, OASPL and Sound Pressure Level, SPL) were obtained. Results were then compared with experimental results from a NASA report [36]. In that report, results of experimental testing of various models of lobed mixers with different operating conditions are reported. and Very good agreement was found between the two. More recently, Brionnaud et al. [22] validated the LBM-based solver XFlow on three aeroacoustic cases used for industrial benchmarking. A duct flow past a thick orifice plate was first simulated. The power spectral density of the axial velocity and pressure was compared to the reference data and similar spectra was obtained. A subsonic jet through a straight pipe was then simulated. A broadband noise of 37 dB and a lower frequency peak around 60 dB were accurately predicted half a meter away from the exit. Finally, the LAGOON two-wheels landing gear test case was benchmarked. The LAGOON is a landing gear noise database and validation case funded by Airbus in 2006, and part of the Benchmark for Airframe Noise Computations (BANC) aeroacoustics database [37, 38, 39]. The averaged pressure coefficients, and velocity profile for both mean and RMS velocity components were obtained and very good agreement established with experimental steady and unsteady aerodynamics F2 wind tunnel measurements [39, 40, 22].

In blood flow (*i.e.* hemodynamics), the LBM makes tracking of microscopic particles straightforward , due to its kinetic representation of the flow as a discrete set of particle populations. In a 2008 report [31], Sun and Munn used it to simulate the interactions between white and red cells as they flow through the vascular network of both normal and tumoral tissue. Parameters such as forces between the cells, their trajectories, and pressure changes were computed. They developed an LBM with the blood modeled as a suspension of particles in a plasma, while accounting for cell-cell and cell-wall interactions. The LBM was deemed reliable for the prediction of blood flow properties in any vessel geometry and blood composition [31]. In another study, Raheed [32] developed a mesoscopic technique based on the D2Q9 LBM to simulate the two-dimensional elastic deformation and displacement of red blood cells under various types of loadings in microvessels. An Immersed Boundary Method (IBM) was used in conjunction with the model, to handle the deformation of the red blood cells. The method was successfully benchmarked for various types flows (i.e Poiseuille flow, channel flow, and flow past obstacles) [32]. The method has also been used for the simulation of pulsatile flow in arteries. In a 2015 article, Vargas and Argenta [33] built an idealized Lattice Boltzmann model to represent pulsatile flow of blood through arteries. The model was then applied to the femoral artery and results compared with those of medical literature. Qualitatively satisfactory results were obtained [33].

The method has also been successfully used to simulate aerodynamics flows. As early as 2009, Kotapati and Chen [23] used the CFD software LBM-based solver PowerFLOW to perform detailed flow and sound simulations complex vehicle geometries. The aerodynamics of the flow over an Ahmed body were first studied. The Ahmed body is a simplified car geometry shown to reproduce flow features such as vortices, separations, and reattachments [41]. Parameters such as the total and component drag were accurately predicted for a large range of rear slant angles. The aeroacoustics of the Daihatsu wedge box, a simplified model of an automotive greenhouse, were then studied. The box can reproduce flow structures linked to pressure fluctuations on the surfaces, similar to those present on the A-pillar and side glass of a vehicle. Noise levels were very accurately predicted by the LBM, up to a frequency of 3000 Hz [23]. The method has also been used for the computation of indoor airflows aerodynamics. In a 2019 article, Han et. al [24] developed an LBM-LES approach

for application to indoor flows. Indoor isothermal, forced-convection flow was simulated for various grid resolutions, relaxation time schemes, and discrete velocity schemes, with both the LBM and the Finite Volume Method (FVM). The LBM and FVM were then compared in terms of computational speed and computational efficiency, and it was found that the LBM was faster when using more cores. In addition, the parallelizing efficiency of the LBM was significantly higher than that of the FVM [24]. More recently, in 2020, an LBM method for generalized curvilinear coordinates was developed by Reyes Barraza and Deiterding [25]. The method was tested on various two-dimensional cases at low Reynolds numbers, including a cylinder and a NACA0012, and it was found to be accurate [25].

Furthermore, the LBM has also been used for the simulation of multi-phase flows. Due to its local and parallelizable capabilities, the LBM enables the modelling of interfaces as well as the interactions between the phases [30]. For instance, in a 2017 study, the LBM was used to simulate casting mold filling, a two-phase liquid metal-gas flow process, and was shown to correctly simulate effects such as the formation of gas bubbles and the air back pressure [30]. In earth soil studies, it was used by Hu et. al [42] to study the thermal performance of phase transition in a saturated, freezing porous soil. Differences in specific heat capacity between the liquid and solid phases, porosity, and thermal diffusivity ratio of the porous medium to the fluid, were investigated [42]. In another report [43], Wang et. al used a couple bonded particle LBM (BPLBM) scheme to study the erosion process of soil particles and their microscopic migration, in granular filters found in earth dams. To account for the fluid/solid interaction, an Immersed Moving Boundary scheme was implemented. Results were found to be in close agreement with empirical data [43].

In porous media flows, the LBM was used by Zhang in 2011 [26] to study the permeability and tortuosity of two-phase isothermal fluid flow in porous media. The Shan-Chen multi-phase model for non-ideal fluids was incorporated, enabling the existence of two-phases in a single substance. Results for phase separation, surface tension, and pipe flow, among others, were validated against existing theoretical and laboratory experiments data. The method was also shown to accurately reproduce the critical flooding phenomena under strong wettability conditions [26]. In 2007, Nabovati and Sousa [27] performed LBM-based flow simulations in two-dimensional random porous media, with randomly placed rectangular obstacles. Values

of permeability and tortuosity were computed and found to be close to those given in the literature [27]. More recently, in 2018, the LBM was used to study the permeability of the flow in various three-dimensional granular porous structures by Gharibi et al [44]. To account for the solid-fluid interactions, a Smoothed Profile Method (SPM) with the LBM-Multi Relaxation Time scheme was used. Permeability results were compared with analytical data, and very good agreement was found [44].

1.6 Motivation

Due to the ever-increasing interest of LBM for jet noise and aeroacoustic studies, two important aspects must be considered for an LBM scheme to be deemed reliable. Firstly, acoustic waves must be preserved for aeroacoustic simulations, and secondly, stability must be ensured at under-resolved simulations.

The simplest formulation of the LBM, the LBM-Single Relaxation Time (LBM-SRT) or LBM-Bhatnagar-Grook-Cross (LBM-BGK), is known to cause instabilities at low viscosities and high wavenumbers due to the use of a single relaxation time τ for all particle populations. An alternative is to use Multi-Relaxation Times (MRT) without additional filtering, which leads to increased computational costs, but enhanced stability. However, some instabilities persists for under-resolved simulations, as will be seen in Chapter 6. Another solution, introduced by [45], is to introduce explicit filtering in conjunction with the BGK. This work seeks to investigate alternative explicit filtering strategies for the Lattice Boltzmann Method. In particular, an explicit filter (*i.e.* SF-7 [46]) was implemented with the MRT. Both a stability analysis and benchmark tests were conduced. A von Neumann analysis was also conducted on the LBM-BGK with an ADM-based explicit filter.

1.7 Objectives

The first objective of this Masters project was to implement a selective filter based on the MRT formulation of the LBM. The second objective was to conduct a stability analysis and quantify the dispersive, dissipative, and stability properties of the explicitely filtered MRT.

The third objective was to benchmark the selective filtered MRT formulation in two- and three dimensions, and compare the results with those of the unfiltered MRT, and both the filtered and unfiltered BGK formualtions. The fourth and final objective was to perform a stability analysis of a filter based on the ADM implemented with the BGK, and quantify its dispersive, dissipative and stability properties.

1.8 Thesis Organization

This thesis is organized as follows. In Chapter 2, the Lattice Boltzmann Method is presented. Different formulations, boundary conditions, and the relation with the Navier-Stokes equations are detailed. In Chapter 3, explicit filtering as a stabilization method for the LBM is described, and various strategies of explicit filtering with the MRT introduced. In the next chapter, Chapter 4, Large Eddy Simulations-based filtering strategies are introduced and an ADM-based differential filter introduced. In Chapter 5, various steps of the von Neumann analysis as applied to the Lattice Boltzmann Method are described. The von Neumann analysis is applied on the LBM-MRT with the SF-7 explicit filter and on the LBM-BGK with the ADM-based filter. In Chapter 6, the LBM-MRT scheme with the SF-7 explicit filter is benchmarked with a two-dimensional dual shear layer and a three-dimensional Taylor-Green vortex test cases. Results are compared for various grid sizes and againsts various schemes. Finally, a conclusion is provided in Chapter 7 with recommendations for future studies.

Chapter 2

Lattice Boltzmann Method

2.1 From the Lattice Gas Automata to the Lattice Boltzmann Method

Although this thesis is concerned with the LBM, the Lattice Gas Automata (LGA) will be first presented, for clarity. Considered as a precursor to the LBM, the LGA was developed by Hardy, Pomeau, and de Pazzis in the 1970's [13]. It was further extended in [47] and [48]. The method consists of a lattice where particles are free to move on links. At each node (*i.e.* "site"), there either is or there is not a particle travelling in a certain direction: this is a boolean description of the lattice. The unknown is the particle population $n_i(x,t)$. It represents the number of particles on each link of a cell:

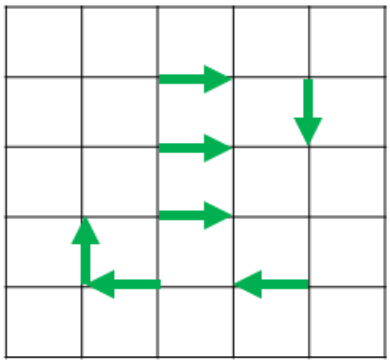

Figure 2.1: Particles on a Lattice Gas Automata Lattice.

2.2 Lattice Boltzmann Method: a Mesoscopic Method

Most traditional Computational Fluid Dynamics methods follow a macroscopic approach; PDE equations such as the Navier Stokes Equations are solved using the Finite Difference (FDM), Finite Element (FEM) or Finite Volume Method (FVM). At the other extreme, one finds the microscopic approach, where molecules are considered individually, the behavior is governed by Hamilton's equation. The LBM constitutes an intermediate approach between the two. In the LBM, groups of molecules are considered and their behavior translated via a particle distribution function, f, which translates the probability of having particles move in a certain direction. The time evolution of f is governed by the Boltzmann Equation. As such, the LBM is classified as a mesoscopic scale method. The LBM has two main advantages. Firstly, boundary Conditions are easy to implement (*i.e.* simple bounce-back rules can be implemented). Secondly, it has a local behavior (*i.e.* particles distributions stream to their neighbors during an iteration). However, it is unsuitable for high Mach numbers due to the presence of an extra term in the Chapman-Enskog expansion (see [18] for more details). Additionally, it requires the use of a completentary scheme in order to model heat flow.

2.3 From Boltzmann Equation to Lattice Boltzmann Equation

The Boltzmann Equation, derived by Ludwig Boltzmann, describes the dynamics of an ideal gas. The motion of particles in space and time is related to macroscopic quantities such as density and velocity. The exchange of momentum and energy among particles is performed via successive streamings and collisions.

The original Boltzmann Equation is given by [15] as

$$\frac{\partial f}{\partial t} + \vec{u} \bullet \nabla f = \Omega, \tag{2.1}$$

with $f(x,t)$ the particle distribution function, $\vec{u}$ the particle velocity, and Ω the collision operator. This equation is valid for an infinite number of dimensions. The LBM simplifies

this idea by introducing a discrete number of streaming directions and confining the particles to move on a lattice: this is the Lattice Boltzmann discretization.

2.4 Discretized Lattice Boltzmann Equation

Typical LBM stencils are defined by DnQm, with n the number of dimensions and m the number of velocities. The three most popular lattice Boltzmann models in one, two and three dimensions are respectively the D1Q3, D2Q9, and D3Q19 stencils. Other existing schemes are the D2Q4 and D2Q7 in two dimensions, and the D3Q15 and D3Q27 in three dimensions. In the D2Q9 model for instance, a particle can move in nine directions, including the central node at rest.

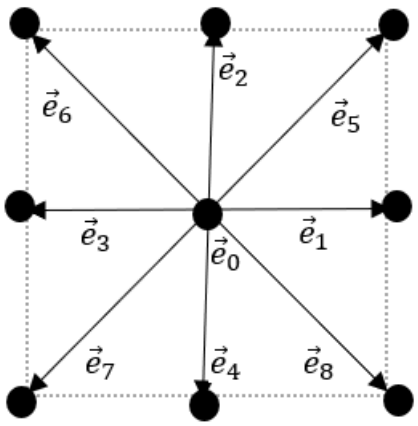

Figure 2.2: Velocities for the D2Q9 lattice model.

The nine velocities $\vec{e_i}$ are expressed as

$$\vec{e_i} = \begin{cases} (0,0) & i = 0 \\ (1,0),(0,1),(-1,0),(0,-1) & i = 1,2,3,4 \\ (1,1),(-1,1),(-1,-1),(1,-1) & i = 5,6,7,8 \end{cases} \tag{2.2}$$

These velocities need to be scaled by the particle propagation speed, c, such that lattice velocities are expressed as $c_i = c\vec{e_i}$. Both the velocities and the number of directions are derived in order to ensure symmetry and Galilean invariance. The particle distribution function $f_i(\vec{x}, t)$ then represents the probability for a particle to stream in either one of the

9 possible directions. It solves the lattice Boltzmann equation, a discretized version of the Boltzmann equation given by

$$f_i(\vec{x} + c\vec{e_i}\Delta t, t + \Delta t) - f_i(x,t) = \Omega_i(x,t), \tag{2.3}$$

for $i = 0, \ldots .Q-1$. The conservation of mass and momentum after particles have collided is ensured by the discrete collision operator, Ω_i. The velocities and weights for each abscissae, i are provided below for the D1Q3, D2Q9 and D3Q19 stencils. For all these velocity sets, the speed of sound is $c_s = 1/\sqrt{3}$.

	i	e_i	w_i
D1Q3	0	(0)	$2/3$
	$1-2$	$(1), (-1)$	$1/6$
D2Q9	0	$(0,0)$	$4/9$
	$1-4$	$(\pm 1, 0), (0, \pm 1)$	$1/9$
	$5-8$	$(\pm 1, \pm 1)$	$1/36$
D3Q19	0	$(0,0,0)$	$4/9$
	$1-6$	$(\pm 1, 0, 0), (0, \pm 1, 0), (0, 0, \pm 1)$	$1/18$
	$7-18$	$(\pm 1, \pm 1, 0), (\pm 1, 0, \pm 1), (0, \pm 1, \pm 1)$	$1/36$

Table 2.1: Velocities and weights for the D1Q3, D2Q9 and D3Q19 stencils.

2.5 Single Relaxation Time (SRT) Formulation

In the LBM, the update from the old ($f_i(x,t)$) to the new distribution functions is ensured by the collision operator, which controls how post-collision populations are updated while ensuring conservation laws are satisfied. Quite complex in the complete detailed mathematical model, it has been simplified by Higuera and Jimenez [49] in 1989. They linearized the collision operator by assuming that the post-collision discrete distribution functions, f_i, are close to their equilibrium value, ${f_i}^{eq}$. The resulting linearized operator is expressed as

$$\Omega_i(\vec{x},t) = -K_{ji}\left(f_i - {f_i}^{eq}\right), \tag{2.4}$$

where K_{ji} are the entries of the collision matrix, K, that regulates how particle populations relax towards equilibrium. In the SRT approach, all particle populations are assumed to relax towards equilibrium at the same rate. The collision matrix K_{ji} has been defined by Bhatnagar-Grook Kroos as [50]

$$K_{ji} = \frac{1}{\tau}. \tag{2.5}$$

This leads to the LBM-BGK or (LBM-SRT) model [16], given as

$$f_i(\vec{x} + c\vec{e_i}\Delta t, t + \Delta t) = f_i(\vec{x},t) + \Omega_i(\vec{x},t), \tag{2.6}$$

with

$$\Omega_i(x,t) = -\frac{1}{\tau}[f_i(x,t) - {f_i}^{eq}(x,t)]. \tag{2.7}$$

In this equation, $f_i(\vec{x},t)$ corresponds to the initial distribution in the domain. The terms $f_i(\vec{x}+c\vec{e_i}\Delta t, t+\Delta t)$ are the updated populations, ${f_i}^{eq}(\vec{x},t)$ is the the equilibrium distribution, and τ is the relaxation time towards equilibrium (*i.e.* the time needed for particle populations to reach their equilibrium values). The lattice speed is equal to

$$c = \Delta x \Delta t. \tag{2.8}$$

For the D2Q9 model, the Chapman-Enskog expansion enables to relate the relaxation time and the kinematic (υ) and bulk (μ_υ) viscosities of the fluid as [45, 19]

$$\upsilon = {c_s}^2\tau - \frac{\Delta t}{2}, \mu_\upsilon = \frac{2}{D}\upsilon, \tag{2.9}$$

with D the number of dimensions (two for the D2Q9 model). The lattice speed of sound, c_s, is defined as $c_s = \frac{c}{\sqrt{3}}$. One notable limitation of the LBM-SRT formulation is that for relaxation times τ close to 0.5 (with $\Delta t = 1$), issues can arise if the viscosity becomes negative, yielding unrealistic results. Another limitation is that the bulk and kinematic

viscosities are linked and thus constrained by each other, which is not physically accurate. Note that equilibrium populations correspond to distribution values in the absence of external excitement. In the BGK formulation, the equilibrium distribution is defined as

$$f_i^{eq}(\vec{x},t) = w_i\rho\left[1 + \frac{1}{{C_S}^2}\left(\vec{c_i} \bullet \vec{u}\right) + \frac{1}{2{C_S}^4}\left(\vec{c_i} \bullet \vec{u}\right)^2 - \frac{1}{2{C_S}^2}\left|\vec{u}\right|^2\right], \tag{2.10}$$

with u the macroscopic velocity and c_s the lattice speed of sound, which is equal to $\frac{1}{\sqrt{3}}$ for the D2Q9 model and defined as

$${c_s}^2 = \sum_{i=1}^{8} w_i c_i c_i. \tag{2.11}$$

The weights w_i are derived such that lattice symmetry is ensured, and are given as:

$$w_i = \begin{cases} 4/9, & i = 0 \\ 1/9, & i = 1,2,3,4 \\ 1/36, & i = 5,6,7,8 \end{cases} \tag{2.12}$$

for an isotropic behavior of the fluid. Finally, the macroscopic density and velocity can be directly calculated taking moments of the distribution function at each node x of the flow,

$$\begin{cases} \rho = \sum_{i=0}^{8} f_i \\ u = \frac{1}{\rho}\sum_{i=0}^{8} c_i f_i \end{cases} \tag{2.13}$$

The equilibrium function given by equation (2.10) is a second-order expansion of the Maxwell-Boltzmann distribution function, which enables to recover the weakly-compressible Navier-Stokes equations.

2.6 LBM algorithm

The term on the left hand-side of equation 2.6 corresponds to the streaming process, while the term on the right-hand side represents the collision process. Starting from an initial distribution of particles $f_i(\vec{x},t)$ at all points in the domain, the populations are first propagated to their neighbors, yielding an intermediary distribution of $f_i(\vec{x},t) \longrightarrow {f_i}^*(\vec{x},t)$ in the domain, which corresponds to the streaming step, with

$$f_i(\vec{x} + c\vec{e_i}\Delta t, t + \Delta t) = f_i^*(x, t). \tag{2.14}$$

Particles are then collided, when they reach the same site at the same time. Post-collision updated distributions $f_i(\vec{x} + c\vec{e_i}\Delta t, t + \Delta t)$ are then computed using equation 2.6 as

$$f_i(\vec{x} + c\vec{e_i}\Delta t, t + \Delta t) = f_i^*(x, t) - \frac{1}{\tau}[f_i^*(x, t) - f_i^{eq}(x, t)]. \tag{2.15}$$

Note that the opposite process can also be adopted: first initialize $f_i(\vec{x}, t)$ in the domain, then compute $f_i{}^*(\vec{x}, t)$ using equation 2.6, and finally set the updated distributions $f_i(\vec{x} + c\vec{e_i}\Delta t, t + \Delta t)$ equal to $f_i{}^*(\vec{x}, t)$. The LBM algorithm consists in first initializing the distributions f, the velocity u, and the density ρ in the domain. Then, the streaming step occurs, with the particles streaming to their neighbors. The distribution function, f, is then updated in the next step. The fourth step is to calculate the updated velocity, u, and density, ρ. The final step is the collision, with the computation of the updated distribution function, f.

The streaming process can be visualized in Figure 2.3.

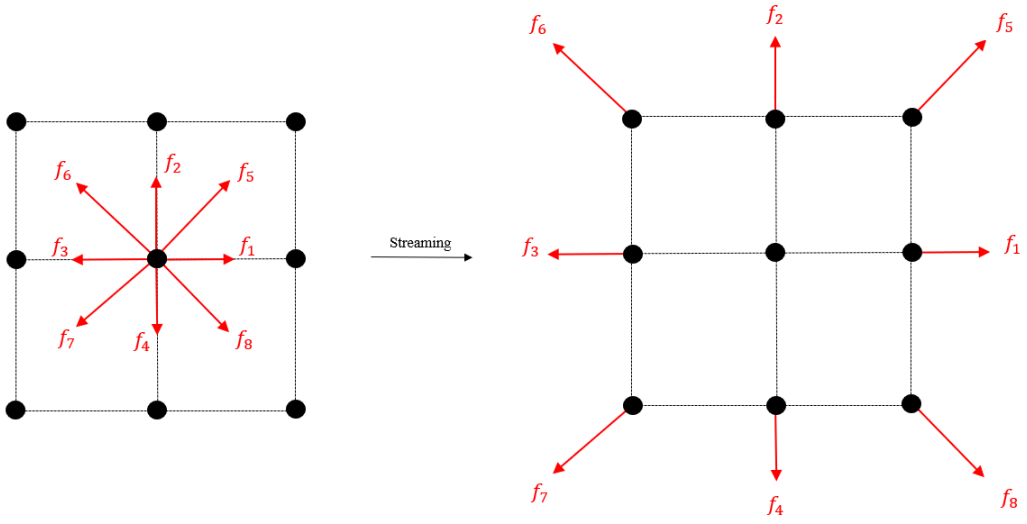

Figure 2.3: LBM streaming process.

2.7 Boundary Conditions (BCs) in LBM

In the LBM, boundary conditions need to be carefuly implemented in order to accurately reproduce the macroscopic boundary conditions. Boundary conditions also play an important role in ensuring the stability and accuracy of the simulation. Some of the most common boundary strategies will be presented: the Bounce-back BCs, the Periodic BCs, and the Zou-He velocity and pressure BCs.

2.7.1 Bounce-Back BCs

Bounce-back boundary conditions simulate a no-slip condition on the boundary. The concept is as follows: when a particle reaches a boundary, it is reflected along the same axis in the opposite direction. The post reflection distributions are obtained by changing the sign of the incoming distributions. Two implementations are possible: 1) on-grid; and 2) mid-grid.

On-grid

In this method, the boundary of the domain is aligned with the nodes. Particles that reach a wall are simply reflected back into the computational domain. The value of the incoming distribution functions (*i.e.* fluid particles) is reversed when these reach the walls. The process is shown below. Note that due to the one-sided nature of the process, this method is first order in accuracy. The process is shown in figure 2.4.

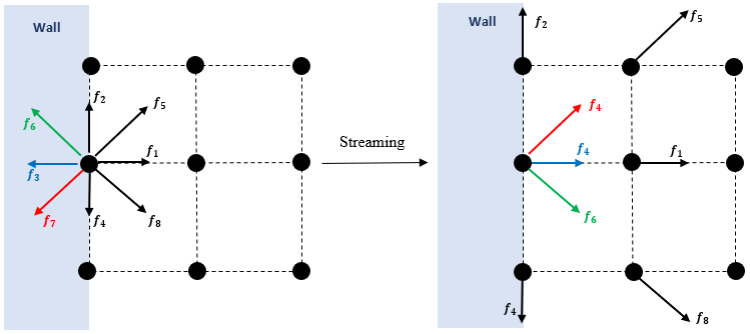

Figure 2.4: LBM on-grid boundary conditions.

Mid-grid

In this configuration, the boundary is placed between real nodes and fictious nodes. Particles first stream to the fictious nodes before colliding and reversing their directions. Finally, bounce-back boundary conditions are implemented on the real nodes. This method is second order in accuracy. The process is shown in figure 2.5.

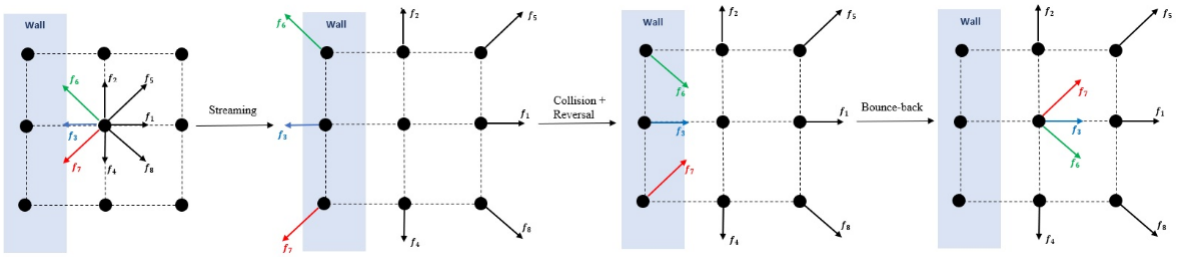

Figure 2.5: LBM mid-grid boundary conditions.

2.7.2 Zou-He BCs

Many simulations require a prescribed pressure (*i.e* density) or velocity at the boundaries. The velocity and pressure boundary conditions were first introduced by Zou and He [51].

The definition is as follows [52]; the velocity $\vec{u}_L(u_x, u_y)$ is first prescribed on the left boundary. After streaming, the known distributions are f_0, f_2, f_3, f_4, f_6, and f_7. f_1, f_5, f_8 and ρ are the unknowns. Zou-He [51] then suggested to form a linear system of f_1, f_5, f_8 and

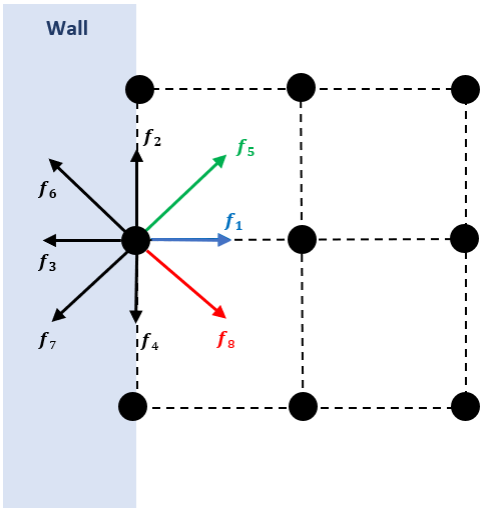

Figure 2.6: LBM Zou-He boundary conditions.

ρ as

$$f_1 + f_5 + f_8 = \rho - (f_0 + f_2 + f_3 + f_4 + f_6 + f_7)\,, \tag{2.16}$$

$$f_1 + f_5 + f_8 = \rho u_x - (f_3 + f_6 + f_7)\,, \tag{2.17}$$

and

$$f_5 - f_8 = \rho u_y - f_2 + f_4 - f_6 + f_7. \tag{2.18}$$

The density ρ is computed from the first two equations as

$$\rho = \frac{1}{1 - u_x}\left[(f_0 + f_2 + f_4 + 2\,(f_3 + f_6 + f_7))\right]. \tag{2.19}$$

To close the system, a fourth equation is needed. It is derived using the assumption that the bounce-back condition still applies to the non-equilibrium part of the distributions that are normal to the boundary. Therefore, it is defined as

$$f_1{}^{neq} = f_3{}^{neq} \Rightarrow f_1 - f_1{}^{eq} = f_3 - f_3{}^{eq}. \tag{2.20}$$

f_1 is obtained from (2.20) and (2.10), and f_5 and f_8 subsequently calculated,

$$f_1 = f_3 + \frac{2}{3}\rho u_y, \tag{2.21}$$

$$f_5 = f_7 - \frac{1}{2}(f_2 - f_4) + \frac{1}{6}\rho u_x + \frac{1}{2}\rho u_y, \tag{2.22}$$

and

$$f_8 = f_6 - \frac{1}{2}(f_2 - f_4) + \frac{1}{6}\rho u_x + \frac{1}{2}\rho u_y \tag{2.23}$$

A similar procedure can be followed for a pressure boundary condition. Taking $u_y = 0$, u_x is defined as

$$u_x = 1 - \frac{[f_0 + f_2 + f_4 + 2(f_3 + f_6 + f_7)]}{\rho}. \tag{2.24}$$

One limitation is that, as the distribution functions are assumed along the normal to the boundary, the Zou-He boundary conditions can be hard to express for complex boundaries. Additionally, the low-compressibility nature of the LBM can cause reflections at the boundaries. To avoid that, approaches such as non-reflecting boundary conditions can be introduced [53, 54].

2.7.3 Periodic BCs

These boundary conditions are straightforward to implement. For a flow circulating from the left to the right, the incoming distributions at left boundary correspond to the outgoing distributions at the right boundaries. The process is shown in figure 2.7.

2.8 Alternative LBM Formulations

2.8.1 Multi-Relaxation Time (MRT formulation)

The single relaxation time formulation of the LBM was shown to consider one single relaxation time, τ, for all distribution functions. This can lead to numerical instabilities as it

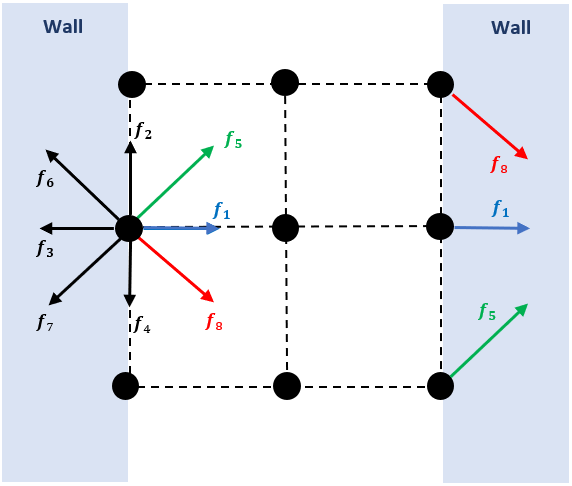

Figure 2.7: LBM periodic boundary conditions.

fails to properly reproduce the macroscopic physics of the flow. In reality, different hydrodynamic variables (*i.e.* such as density, and x- and y- momentum) relax towards equilibrium at different rates. Recall that macroscopic variables can be recovered by taking moments of different orders of the distribution function, f_i, at each point in the flow. To stabilize the LBM, one strategy is to convert f_i to the moments m_i, perform the collision process, and revert back to the f_i for the streaming step. Doing so enables to use a different relaxation time, τ_i, for each moment, m_i.

The LBM-MRT equation is expressed as

$$f_i(\vec{x} + c\vec{e_i}\Delta t, t + \Delta t) - f_i(x,t) = M^{-1}SM[f_i(x,t) - f_i{}^{eq}(x,t)]. \tag{2.25}$$

For the D2Q9 stencil, moments are obtained as: $m_i = Mf_i(\vec{x}, t)$, with

$$M = \begin{pmatrix} 1 & 1 & 1 & 1 & 1 & 1 & 1 & 1 & 1 \\ 0 & 1 & 0 & -1 & 0 & 1 & -1 & -1 & 1 \\ 0 & 0 & 1 & 0 & -1 & 1 & 1 & -1 & -1 \\ -4 & -1 & -1 & -1 & -1 & 2 & 2 & 2 & 2 \\ 0 & 1 & -1 & 1 & -1 & 0 & 0 & 0 & 0 \\ 0 & 0 & 0 & 0 & 0 & 1 & -1 & 1 & -1 \\ 0 & -2 & 0 & 2 & 0 & 1 & -1 & -1 & 1 \\ 0 & 0 & -2 & 0 & 2 & 1 & 1 & -1 & -1 \\ 4 & -2 & -2 & -2 & -2 & 1 & 1 & 1 & 1 \end{pmatrix}. \tag{2.26}$$

The first moment corresponds to density and can be recovered as follows for example,

$$\rho = \sum_{i=0}^{8} M_{1j} f_j = \sum_{i=0}^{8} 1 * f_j. \tag{2.27}$$

The term S is a diagonal matrix where each diagonal entry τ_i corresponds to the relaxation time of the moment m_i. In the MRT formulation, collision is performed in the momentum space, while streaming is performed on the original distributions. In other words, the distributions are first converted to moments via

$$\mathbf{m} = M\mathbf{f}, \tag{2.28}$$

where $\mathbf{m}$ is the vector of moments and $\mathbf{f}$ is the vector of distribution functions. These moments are then collided. We then recover the original distributions as

$$\mathbf{f} = M^{-\mathbf{1}}\mathbf{m}. \tag{2.29}$$

The Chapman-Enskog expansion applied to the MRT scheme yields independent kinematic (*i.e.* ν) and bulk (i.e μ_B) viscosities [55],

$$\nu = {c_s}^2(\frac{1}{s_4} - \frac{\Delta t}{2}) = {c_s}^2(\frac{1}{s_4} - \frac{\Delta t}{2}), \tag{2.30}$$

and

$$\mu_B = \frac{2}{D}{c_s}^2\frac{1}{s_3} - \frac{\Delta t}{2}. \tag{2.31}$$

It will be shown that this ability to increase the bulk viscosity is what makes the MRT more stable than the BGK formulation. Indeed, an increase of the bulk viscosity via a modification of s_3 can damp spurious waves.

The derivation of the transformation matrix M in two dimensions (D2Q9) and three dimensions (D3Q9) is presented in the Appendix.

2.8.2 Regularized LBM

The idea behind the regularized BGK (RBGK) is to enhance stability by removing higher order, non-hydrodynamic terms from the particle populations. It stems from the observation that, in the Hermite polynomial expansion of the distribution function, only the first three terms are needed to recover the macroscopic equations (*i.e.* Navier-Stokes) and terms (density, velocity, and stress tensors).

The LBE-BGK equation is given by

$$f_i(\vec{x} + c\vec{e_i}\Delta t, t + \Delta t) = f_i * (x,t) - \frac{1}{\tau}[f_i * (x,t) - {f_i}^e q(x,t)]. \tag{2.32}$$

The distribution ${f_i}^*$ is reconstructed from the incoming distributions as

$${f_i}^* = \frac{w_i}{2{c_0}^4}\left(\xi_{i\alpha}\xi_{i\beta} - {c_0}^2\delta_{\alpha\beta}\right)\sum_j \xi_{i\alpha}\xi_{i\beta}\left(f_i - {f_i}^{eq}\right). \tag{2.33}$$

The collision step is then performed using these regularized distributions. This results in the regularized Lattice Boltzmann equation,

$$f_i(\vec{x} + c\vec{e_i}\Delta t, t + \Delta t) = {f_i}^e q(x,t) + \frac{(1-\frac{1}{\tau})w_i}{2{c_0}^4}(\xi_{i\alpha}\xi_{i\beta} - {c_0}^2\delta\alpha\beta)\sum_j \xi_{i\alpha}\xi_{i\beta}(f_i - {f_i}^e q). \tag{2.34}$$

2.8.3 Entropic LBM

The entropic implementation of the LBM is a modification of the LBM-BGK formulation and reads

$$f_i(\vec{x} + c\vec{e_i}\delta t, t + \Delta t) = f_i * (x,t) - \alpha\beta[f_i * (x,t) - {f_i}^e q(x,t)]. \tag{2.35}$$

The main differences lie in the computation of the equilibrium distribution function ${f_i}^{eq}$ and a modification of the relaxation time, α and β. The distribution ${f_i}^{eq}$ is calculated by considering an entropy function,

$$H(f) = \sum_{i=0}^{8} f_i ln\left(\frac{f_i}{\omega_i}\right), \tag{2.36}$$

with ω_i the weighting coefficients. The distribution ${f_i}^{eq}$ can be computed from the minimal value of $H(f)$ that is reached at equilibrium. The maximal over-relaxation coefficient is obtained from the positive root of the entropy condition as

$$H(f + \alpha\left(f^{eq} - f\right)) = H(f). \tag{2.37}$$

Chapter 3

Explicit Filtering as a Stabilization Method

In Ricot et al. [27], it is explained that instabilities occur in regions where the nonequilibrium distribution parts are too large. Hence, filtering them will lead to enhanced stability. In this approach, filtering is thus performed on the collision operator non equilibrium part of distributions (f_i–$f_i^{eq} = f_i^{neq}$),

$$-\frac{1}{\tau}\overline{f_i(x,t) - f_i^{eq}(x,t)} = -\frac{1}{\tau}\overline{f_i^{neq}(x,t)}. \tag{3.1}$$

The filtered post-collision distributions are

$$f_i(x + \Delta x, t + \Delta t) = f_i(x,t) - \frac{1}{\tau}\overline{f_i^{neq}(x,t)}. \tag{3.2}$$

These are then used to compute the macroscopic variables. The general expression of the explicit filtering of a variable Φ is given by [27]

$$\overline{\Phi(x)} = v\,(x) - \sigma \sum_{j=1}^{D} \sum_{n=-N}^{N} d_n \Phi(x + n x_j). \tag{3.3}$$

In this equation, σ is the filter strength, comprised between 0 and 1, D the number of dimensions, N the number of stencil points, and d_n the stencil coefficients. The non-local filtering action dissipates the spurious small scales while keeping the large scale acoustic waves unaffected. The filter must be symmetrical in order to avoid dispersive errors [45]. To

this end, the coefficients are defined such that $d_n = d_{-n}$. In order to derive the coefficients, d_n, the Taylor expansion of the previous equation is first obtained, and the terms obtained then cancelled [56]. An ideal filter should leave oscillations in the low wavenumber range unaffected and have a sharp cut off at high wavenumbers. To this end, Tam *et al.* [57] optimized the coefficients d_n in the Fourier space for a 7-point stencil. Some explicit filters are presented below. Their coefficients are given in the Appendix.

Author	Number of Points	Designation
Skordos [46]	5	SF-5
Skordos	7	SF-7
Tam *et al.* [57]	7	Tam-7
Bogey and Bailly [58]	9	Bogey-9
Bogey and Bailly	11	Bogey-11
Bogey and Bailly	13	Bogey-13

Table 3.1: Summary of Explicit Filters.

In the Lattice Boltzmann approach, three strategies exist. The first consists in a filtering of the distribution functions (or moments for MRT). The second consists in filtering of the collision operator, which results in the highest cut-off wavenumber as shown by [45] for the BGK operator. The third approach is to filter the macroscopic variables.

The derivation of the filtered equations and the amplification matrices for the BGK case is detailed in [45]. Here the same procedure will be followed but for the MRT case. Recall that the LBM-MRT equation is given as

$$f_i(\vec{x} + c\vec{e_i}\Delta t, t + \Delta t) - f_i(x,t) = M^{-1}SM[f_i(x,t) - f_i{}^{eq}(x,t)]. \tag{3.4}$$

This can be re-expressed as:

$$f_i(\vec{x} + c\vec{e_i}\Delta t, t + \Delta t) = f_i(x,t) + M^{-1}S[m_i(x,t) - m_i{}^{eq}(x,t)]. \tag{3.5}$$

3.1 Filtering of the distribution function

The first idea consists in calculating the updated distribution functions $f_i(\vec{x} + c\vec{e_i}\delta t, t + \Delta t)$ using equation (3.5), then calculating their filtered values as

$$\bar{f_i}(\vec{x}, t) = f_i(\vec{x}, t) - \sigma \sum_{j=1}^{n} \sum_{n=-N}^{N} d_n f_i(\vec{x} + n x_j, t). \tag{3.6}$$

The filtered macroscopic variables can then be calculated using equation (2.13). For the density and momentum this yields

$$\bar{\rho} = \sum_{i=0}^{8} \overline{f_i}, \tag{3.7}$$

and

$$\rho \bar{u}_i = \sum_{i=0}^{8} c_i \overline{f_i}. \tag{3.8}$$

The expression for the fully filtered lattice Boltzmann equation is then given as

$$f_i(\vec{x} + c\vec{e_i}\Delta t, t + \Delta t) = f_i(x, t) - M^{-1} S M [f_i(x, t) - f_i^e q(x, t)]. \tag{3.9}$$

The application of the von Neumann analysis on this equation then yields the amplification matrix, $M^{\bar{f}_i}$, of the problem as

$$M^{\bar{f}_i} = (1 - \sigma f) A^{-1} \left[I - M^{-1} S M N^{BGK} \right]. \tag{3.10}$$

The filter function, f, (not to be confused with the distribution functions, f_i) is itself defined as [45]

$$f = \sum_{j=1}^{n} \sum_{n=-N}^{N} d_n e^{ink \cdot x_j}. \tag{3.11}$$

3.2 Filtering of the macroscopic variables

In the fully filtered lattice Boltzmann equation, both the distribution function and the macroscopic variables are filtered. An alternative is to only filter the macroscopic variables,

which leads to a subsequent decrease in computational costs as the filtered distribution functions need not be calculated at every iteration. The steps consist in first computing the updated distribution functions using equation (3.5), then calculating the macroscopic variables from these functions with equations (2.13). Finally, the macroscopic variables are filtered using equation (3.3). For instance, the density and momentum are computed as

$$\begin{cases} \overline{\rho(x,t)} = \rho(x,t) - \sigma \sum_{j=1}^{n} \sum_{n=-N}^{N} d_n \rho(x + nx_j, t), \\ \overline{\rho u_i(x,t)} = \rho u_i(x,t) - \sigma \sum_{j=1}^{n} \sum_{n=-N}^{N} d_n \rho u_i(x + nx_j, t). \end{cases} \tag{3.12}$$

The filtered macroscopic values are used to calculate the filtered equilibrium distribution function as

$$\overline{f_i{}^{eq}(\vec{x},t)} = w_i \overline{\rho} \left[1 + \frac{1}{{C_S}^2} \left(\vec{c_i} \bullet \overline{\vec{u}} \right) + \frac{1}{2{C_S}^4} \left(\vec{c_i} \bullet \overline{\vec{u}} \right)^2 - \frac{1}{2{C_S}^2} \left| \overline{\vec{u}} \right|^2 \right]. \tag{3.13}$$

The filtered velocities $\overline{\vec{u}}$ are calculated as

$$\overline{\vec{u}} = \frac{\overline{\rho u_i(x,t)}}{\overline{\rho(x,t)}}. \tag{3.14}$$

Finally, the amplification matrix can be computed as

$$M^{\overline{m_i}} = A^{-1} \left[I - M^{-1} S M (I - (1 - \sigma f) F^{eq}) \right]. \tag{3.15}$$

3.3 Filtering of the collision operator

In both the first and second approaches, the non-equilibrium part of the moments ${m_i}^{neq} = m_i - {m_i}^{eq}$ is not directly filtered. In high shear regions of the flow, where the distribution functions and therefore the moments evolve too far from the equilibrium value, ${m_i}^{eq}$, instabilities can occur. It then makes sense to apply the filter on the non-equilibrium part of the moments in the collision operator. The moments are first filtered as

$$\overline{{m_i}^{neq}(\vec{x},t)} = {m_i}^{neq}(\vec{x},t) - \sigma \sum_{j=1}^{n} \sum_{n=-N}^{N} d_n {m_i}^{neq}(\vec{x} + n\vec{x_j}, t). \tag{3.16}$$

This yields a filtered collision operator,

$$- M^{-1}SM[\overline{m_i{}^{neq}(\vec{x},t)}]. \tag{3.17}$$

Finally, the new distribution functions are obtained via

$$f_i(\vec{x} + c\vec{e_i}\Delta t, t + \Delta t) = fi(x,t) - M^{-1}SM[m_i{}^{neq}(x,t)]. \tag{3.18}$$

The macroscopic variables are then calculated using $f_i(\vec{x} + c\vec{e_i}\Delta t, t + \Delta t)$ and equation (2.13). In their work, Ricot *et al.* [45] applied four filters (SF-5, SF-7, Tam-7 and Bogey-9) on the fully filtered LBM with the BGK collision operator. Then, they studied the dissipation of the shear mode and positive acoustic mode in order to compare the cut-off wavenumbers of the different filters. It was found that the SF-7 filter has a higher cut-off wavenumber than the SF-5 filter, which uses less stencil points. Overall, the best filter was found to be Bogey-9 which is non-dissipative up until a wavenumber k of approximately $\frac{\pi}{2.3}$. On the other hand, Tam-7 is the most inefficient filter with a dissipation that is too high at low wavenumbers. Recall that an ideal filter should leave low wavenumber oscillations unaffected while having a sharp cut-off at high wavenumbers. Due to the high computational cost of the Bogey-9 scheme, SF-7 was found to be a good compromise between efficiency and computational costs and was used for the rest of the von Neumann analysis. In accordance with Ricot *et al.* [45], the following analysis for the LBM-MRT scheme will be performed with the 7-point stencil by Skordos [46], SF-7.

Chapter 4

Large Eddy Simulations with LBM

4.1 Subgrid scale Modeling in LES

Large Eddy Simulations consist of the direct computation of large scales of turbulence, and the modeling of subgrid scales, which cannot be captured by the spatial resolution of the grid. The smallest grid size is commonly referred to as "grid cut-off". This is in part motivated by the need to reduce computational costs to acceptable levels, and by physical considerations: the smallest eddies are almost isotropic and display a universal behavior. On the other hand, the larger eddies have an anisotropic behavior which is greatly influenced by the domain size. Turbulence models seek to represent the dissipative effect of SGS scales on the flow and can be divided into two main approaches: functional modeling and structural modeling. In LES, the unknowns are the unfiltered field variables, ϕ. The filtered variables to be solved for are $\bar{\phi}$ and are obtained via the application of a low pass spatial filter. Functional and structural modeling differ in how ϕ is recovered. Functional models start by filtering the governing equations and express the additional term T_{ij} (*i.e.* defined in the introduction) in terms of the filtered variables and an eddy viscosity. Structural models on the other hand seek to reconstruct ϕ from $\bar{\phi}$ via a deconvolution process,

$$\Phi \approx \Phi^* = D * \overline{\Phi}, \tag{4.1}$$

with D the deconvolution operator.

4.2 Functional Modeling

The effect of subgrid scales on resolved scales can be seen as an additional viscosity which effectively dissipates the turbulent kinetic energy. This additional viscosity is called the "eddy viscosity". The viscosity of the flow can then be extended to yield a turbulent viscosity. For reliable results, the turbulent kinetic energy must be dissipated at a correct rate by the model. Functional models are divided into implicit and explicit approaches. As a reminder, in the implicit LES (ILES), the grid size is implicitly considered as the grid cutoff, such that any wavenumber smaller than the grid cut-off wavenumber $k_{gco} = \pi\Delta x$ is not represented. By introducing a truncation error, the dissipative effect of SGS can me mimicked, and no additional terms are needed. While computationally efficient, as no additional terms are needed, implicit methods are also more prone to aliasing where the energy is transferred from non-resolved to resolved scales, leading to an energy build-up at the grid cut-off wavenumber. In the explicit LES approach, the eddy viscosity is directly expressed as a function of the strain rate tensor. Expressing the SGS terms explicitly as a function of the filtered values, $\bar{\phi}$ gives more control about the filter definition and parameters.

4.3 Structural Modeling

Structural modeling approaches aim to reconstruct the unfiltered scales via a decomposition of the scales. These include multi-scale, regularization, and deconvolution based methods [59]. Structural modeling approaches start by decomposing the unfiltered flow into a resolved and non-resolved scales,

$$\phi = \bar{\phi} + \phi', \tag{4.2}$$

with $\bar{\phi}$ the resolved, filtered scales and ϕ'

the non-resolved scales. Resolved scales correspond to scales bigger than or equal to the grid size, which acts as the effective spatial filter. These filtered scales are given by the filtered Navier-Stokes equations presented earlier and which read, for incompressible flow,

$$\frac{\partial \overline{u_i}}{\partial t} = 0, \tag{4.3}$$

for the conservation of mass, and

$$\frac{\partial \overline{\rho u_i}}{\partial t} + \overline{\frac{\partial u_i u_j}{\partial x_j}} = -\frac{1}{\rho}\frac{\partial \bar{p}}{\partial x_i} + \nu \frac{\partial^2 \overline{u_i}}{\partial x_j \partial x_j}, \tag{4.4}$$

for the conservation of momentum. In the introduction, we defined the term T_{ij} as $T_{ij} = \overline{u_i u_j} - \bar{u}_i \bar{u}_j$. The term $\overline{u_i u_j}$ can then be decomposed as

$$\overline{u_i u_j} = T_{ij} + \bar{u}_i \bar{u}_j \Longrightarrow \overline{u_i u_j} = (\overline{\bar{u}_i \bar{u}_j} - \bar{u}_i \bar{u}_j) + \left(\overline{u_i' \overline{u_j}} + \overline{\overline{u_i} u_j'}\right) + \overline{u_i' u_j'} + \bar{u}_i \bar{u}_j. \tag{4.5}$$

The term

$$L_{ij} = (\overline{\bar{u}_i \bar{u}_j} - \bar{u}_i \bar{u}_j), \tag{4.6}$$

is known as the Leonard tensor, the term

$$C_{ij} = \left(\overline{u_i \overline{u_j}} + \overline{\overline{u_i} u_j'}\right), \tag{4.7}$$

as the Cross-stress tensor, and the term

$$R_{ij} = \overline{u_i' u_j'}, \tag{4.8}$$

as the Reynolds tensor.

The term can be expressed as:

$$\overline{u_i u_j} = L_{ij} + C_{ij} + R_{ij} + \bar{u}_i \bar{u}_j \tag{4.9}$$

The problem now consists in determining how to compute $L_{ij} + C_{ij} + R_{ij}$. Various approaches exist. In multiscale modeling, equations for all scales are directly solved. Regularization methods use a deconvolution procedure on the regularized Navier-Stokes equations. Finally, approximate deconvolution-based models (ADM) consist in the reconstruction of the smallest scales with a deconvolution approach [59]. A deconvolution operator should be

chosen for the spatial filtering step. As seen before, scales can be divided into resolved and non-resolved scales,

$$\phi = \bar{\phi} + \phi'. \tag{4.10}$$

Instead of directly computing ϕ'

, the deconvolution approach consists in reconstructing ϕ from $\bar{\phi}$. For a variable ϕ, filtering can be seen as a convolution, with

$$\bar{\phi} = G * \phi. \tag{4.11}$$

The goal is to define D such that

$$\phi \approx \phi^* = D * \bar{\phi}, \tag{4.12}$$

which is an approximate deconvolution since $D \approx G^{-1}$.

4.4 Filters for Approximate Deconvolution Models

Approximate deconvolution models are based on a low-pass filtering approach. Adequate filters are thus mandatory for the correct reconstruction of the desired scales. For an ideal filter, the transfer function must have a high grid cut-off wavenumber, removal of all the energy above the grid cut-off, no amplification of any resolved wavenumbers and a sharp decrease at the grid cut-off[59].The last requirement is to avoid a discrepancy between the theoretical and effective cut-off wavenumber.

Filters mainly fall into two categories: discrete filters and differential filters. Filters of the differential type such as elliptic and parabolic filters were first introduced by Germano [60, 61]. In these approaches the filtering involves solving either an elliptical or parabolic differential equation. The main advantage is the possibility to apply the filter on both structured and unstructured grids. Germano's [61] differential filter is given by

$$\bar{\phi} - \sigma^2 \frac{\partial^2 \bar{\phi}}{\partial x_j \partial x_j} = \phi, \tag{4.13}$$

where the parameter σ controls the strength of the filter. The filter's transfer function is obtained as

$$T(k) = \frac{1}{1 + \sigma^2 k^2}. \tag{4.14}$$

While stable (*i.e.* $|T(k)| \leq 1$ for all wavenumbers k), the filter transfer function does not go to zero at the grid cutoff, making the filter potentially unstable as energy is not completely removed from the subgrid scales. This can lead to aliasing where excess energy is stored at wavenumbers just before the grid cutoff, due to a lack of dissipation. Building up on Germano's work, Najafi-Yazdi *et al.*'s [62] proposed a filter in the form of an elliptic partial differential equation (PDE). The filter is significantly less dissipative and leads a complete attenuation of fluctuations at the grid cut-off wavenumber. The filter in differential form is given by

$$\bar{\phi} + \frac{\partial}{\partial x_i}\left(\alpha \frac{\partial \bar{\phi}}{\partial x_i}\right) = \phi + \frac{\partial}{\partial x_i}\left(\beta \frac{\partial \phi}{\partial x_i}\right), \tag{4.15}$$

where α and β are two non-dimensional, free parameters, and x_i is the local coordinate system in the reference computational domain [62]. Parameter α controls the filter shape (*i.e.* the rate of decrease towards zero of the filter and its cut-off wavenumber), while parameter β ensures a full attenuation at the grid cut-off and is determined after the differential equation has been discretized [62]. The filter can be extended to multiple dimensions through mapping from the computational domain to the physical domain, one element at a time. A weak formulation with a test function, w, and a Galerkin projection are then applied; the Finite Element Methods (FEM) discretization is then defined as

$$\mathbf{M}\bar{\phi} = \mathbf{N}\phi. \tag{4.16}$$

The shape functions of a bilinear quadrilateral element are defined as follows, with (ξ, η) the reference coordinate system,

$$N_1 = \frac{1}{4}(1-\xi)(1-\eta), \tag{4.17}$$

$$N_2 = \frac{1}{4}(1+\xi)(1-\eta), \tag{4.18}$$

$$N_3 = \frac{1}{4}(1+\xi)(1+\eta), \tag{4.19}$$

and

$$N_4 = \frac{1}{4}(1-\xi)(1+\eta). \tag{4.20}$$

The filter coefficients are then defined as [59]

$$m_{k,l}{}^{(e)} = \int (N_k N_l)\, d\Omega^{(e)} - \int \left[\frac{\partial N_k}{\partial x_i} \frac{\partial N_l}{\partial x_i} \left(\sum_k \alpha_k N_k \right) \right] d\Omega^{(e)}, \tag{4.21}$$

and

$$n_{k,l}{}^{(e)} = \int (N_k N_l)\, d\Omega^{(e)} - \int \left[\frac{\partial N_k}{\partial x_i} \frac{\partial N_l}{\partial x_i} \left(\sum_k \beta_k N_k \right) \right] d\Omega^{(e)}, \tag{4.22}$$

where $m_{k,l}{}^{(e)}$ describes the effect of node l on node k in the element e. Let a quadrilateral element as seen on Figure 4.1 below. Analysis will be performed for node 1, without loss of generality.

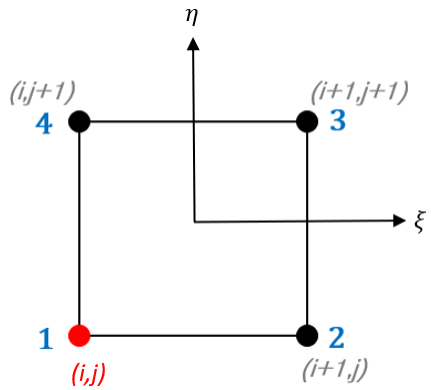

Figure 4.1: Quadrilateral Element.

The left- and right-hand side of the filter for node 1 are respectively given by [59]

$$M^{(e)}\phi = {m_{1,1}}^{(e)}\phi_1 + {m_{1,2}}^{(e)}\phi_2 + {m_{1,3}}^{(e)}\phi_3 + {m_{1,4}}^{(e)}\phi_4, \tag{4.23}$$

and

$$N^{(e)}\phi = {n_{1,1}}^{(e)}\phi_1 + {n_{1,2}}^{(e)}\phi_2 + {n_{1,3}}^{(e)}\phi_3 + {n_{1,4}}^{(e)}\phi_4. \tag{4.24}$$

It can be shown, via analysis, that [62]

$${m_{1,1}}^{(e)} = \frac{1}{36}\left(16 - 9\alpha_1 - 6\alpha_2 - 3\alpha_3 - 6\alpha_4\right), \tag{4.25}$$

$${m_{1,2}}^{(e)} = \frac{1}{36}\left(8 + 3\alpha_1 + 3\alpha_2\right), \tag{4.26}$$

$${m_{1,3}}^{(e)} = \frac{1}{9} + \frac{1}{12}\left(\alpha_1 + \alpha_2 + \alpha_3 + \alpha_4\right), \tag{4.27}$$

and

$${m_{1,4}}^{(e)} = \frac{1}{36}\left(8 + 3\alpha_1 + 3\alpha_2\right). \tag{4.28}$$

Similarly,

$${n_{1,1}}^{(e)} = \frac{1}{36}\left(16 - 9\beta_1 - 6\beta_2 - 3\beta_3 - 6\beta_4\right), \tag{4.29}$$

$${n_{1,2}}^{(e)} = \frac{1}{36}\left(8 + 3\beta_1 + 3\beta_2\right), \tag{4.30}$$

$${n_{1,3}}^{(e)} = \frac{1}{9} + \frac{1}{12}\left(\beta_1 + \beta_2 + \beta_3 + \beta_4\right), \tag{4.31}$$

and

$${n_{1,4}}^{(e)} = \frac{1}{36}\left(8 + 3\beta_1 + 3\beta_2\right). \tag{4.32}$$

We observe that ${m_{1,2}}^{(e)} = {m_{1,4}}^{(e)}$ and ${n_{1,2}}^{(e)} = {n_{1,4}}^{(e)}$ due to symmetry requirements. The z-transform is first applied to the right-hand side of equation (4.24), followed by conditions

for full attenuation. This results in a system of equations for the parameters β_i. Setting $\beta_1 = 1$, one obtains $\beta_2 = \beta_4 = -\frac{2}{3}$ and $\beta_3 = 2$ [59]. This yields

$$n_{1,1}{}^{(e)} = n_{1,2}{}^{(e)} = n_{1,3}{}^{(e)} = n_{1,4}{}^{(e)} = 1. \tag{4.33}$$

The parameters α_i are obtained from β_i with the stability conditions shown in table 4.1.

β_i	α_i
β_1	$\frac{\alpha_1}{\beta_1} = 1$
β_2	$\frac{\alpha_2}{\beta_2} > 1$
β_3	$\frac{\alpha_3}{\beta_3} < \frac{\alpha_2}{\beta_2}$
β_4	$\frac{\alpha_4}{\beta_4} > 1$

Table 4.1: Stability conditions for β_i and α_i parameters.

For the von Neumann Analysis of the LBM scheme with the ADM filter, the tested sets of values are given in table 4.2.

β_i	α_i
$\frac{\alpha_1}{\beta_1}$	1
$\frac{\alpha_2}{\beta_2}$	1.1
$\frac{\alpha_3}{\beta_3}$	1.05
$\frac{\alpha_4}{\beta_4}$	1.1

Table 4.2: BGK ADM von Neumann Analysis filter parameters - Set 1.

Chapter 5

Linear Stability Analysis

Linear stability consists in analyzing the response of a linear system subjected to a disturbance. In particular, the temporal growth rate of the disturbance and its wavenumber need to be computed in time. The von Neumann analysis studies the dispersion and dissipation errors of an initial solution propagated by a numerical scheme. The method was first used for the LBM by Sterling and Chen [63] who linearized the BGK collision operator around a mean flow. More recently, Wissock *et al.* conducted a spectral analysis of the LBM [64]. An ideal numerical scheme possesses two main characteristics: 1) it should not amplify the solution and; 2) should conserve the wavenumbers of each wave. This chapter is divided in three parts. In the first part, the von Neumann analysis methodology is presented in the context of the LBM. In the second part, four collision operators are compared: 1) the BGK; 2) the MRT-RM; 3) the MRT-RM with the SF-7 explicit filter and finally; 4) MRT-RM with the ADM explicit filter.

5.1 von Neumann Stability Analysis

In the Lattice Boltzmann formulation, the procedure consists in decomposing the particle distribution function, f_i, into the sum of an equilibrium state, $\left(\overline{f_i}\right)$, and a perturbation, $(f_i{}')$,

$$f_i = \overline{f_i} + f_i{}'. \tag{5.1}$$

The first term, $\overline{f_i}$, only depends on the average density and velocity and is time and

space invariant. The second term, $f_i{}'$, represents fluctuations from the equilibrium state. The main goal is to obtain a linear equation for the fluctuations, $f_i{}'$, from which we can analyze if the fluctuations are amplified or not. Equation (5.1) is substituted into equation (2.4) and ${f_i}^{eq}$ expanded by the means of a Taylor series centered on f , yielding

$$\Omega_j \approx K_{ji}\left[\left(\overline{f_i} + \frac{\partial {f_i}^{eq}}{\partial f_j}|_{\overline{f_i}} f_i{}'\left(x,t\right) + O\left({f_i}'^2\left(x,t\right)\right)\right) - \left(\overline{f_i}\left(x,t\right) + f_i{}'\left(x,t\right)\right)\right]. \tag{5.2}$$

Substituting equations (5.1) and (5.2) into equation (2.3) gives

$$\overline{f_i}(\vec{x} + c\vec{e_i}\Delta t, t + \Delta t) + f_i'(x + c\vec{e_i}\Delta t, t + \Delta t) - f_i + f_i' = K_{ji}[(\overline{f_i} + \frac{\partial {f_i}^{eq}}{\partial f_j}|_{\overline{f_i}} + O({f_i}^2(x,t))) - (\overline{f_i}(x,t) + f_i{}'(x,t))], \tag{5.3}$$

and

$$f_i(\vec{x} + c\vec{e_i}\Delta t, t + \Delta t) - f_i(x,t) = \Omega_i(x,t). \tag{5.4}$$

This is simplified as (ignoring the higher order terms)

$$f_i{}'(\vec{x} + c\vec{e_i}\Delta t, t + \Delta t) - f_i'(x,t) = K_{ji}(\frac{\partial {f_i}^{e}q}{\partial f_j}|_{f_i} f_i'(x,t) - f_i'(x,t)). \tag{5.5}$$

This is a linear equation, and we assume plane wave solutions of the form

$$f_i{}'\left(x,t\right) = A_i e^{i(kx-\omega t)}, \tag{5.6}$$

where A_i is the amplitude of the sinusoidal wave, $k = k_x, k_y, k_z$ its wavenumber and ω the frequency in time. Substituting equation (5.6) in equation (5.5) gives a linearized LBE-BGK equation in form of an eigenvalue problem:

$$e^{-i\omega}A = MA, \tag{5.7}$$

where is M the amplification matrix defined as $M = A^{-1}\left[I - \frac{1}{\tau}N\right]$ in the BGK case, with I the identity matrix and A and N defined as [45]

$$A_{ij} = e^{ik \cdot c_i} \delta_{ij}, \tag{5.8}$$

and

$$N_{ij} = \delta_{ij} - {F_{ij}}^{eq}, \tag{5.9}$$

with

$${F_{ij}}^{eq} = \left. \frac{\partial f_i}{\partial f_j} \right|_{f_i = {f_i}^{eq}}. \tag{5.10}$$

An eigenvalue analysis of the matrix using a mathematical software such as *Mathematica* [65] yields information about the growth rate and dispersive properties of the modes that correspond to perturbations around the equilibrium solution $\overline{f_i}$. In previous work, Lallemand and Luo [66] used successive approximations of the matrix A_{ij} in terms of the wavenumber, k, and solved the problem analytically. The wavenumber vector k is equal to the number of grid points per wavelength.

Additionally, the eigenvalues are defined as:

$$\lambda = e^{-i\omega}. \tag{5.11}$$

The transport coefficients of the modes ω correspond to their angular frequency and can be obtained as

$$\omega = i \; ln(\lambda). \tag{5.12}$$

These coefficients are complex, and therefore, can be written in the form

$$\omega = \omega_R + i \; \omega_I. \tag{5.13}$$

We can now rewrite the eigenvalues λ as

$$\lambda = e^{-i(\omega_R + i \; \omega_I)} = e^{-i\omega_R} e^{\omega_I}. \tag{5.14}$$

As $|e^{-i\omega_R} = 1|$, we conclude that the real part of ω, ω_R, is linked to dispersion while the imaginary part, ω_I, is related to dissipation. Finally, the stability condition states that perturbations should not be amplified by the scheme, *i.e.*: $|\lambda| \leq 1$. Therefore, analyzing $|\lambda|$ for different wavenumbers helps determinate the scheme's stability.

In summary, the amplification matrix for the BGK case is [45]

$$M^{BGK} = A^{-1}\left[I - \frac{1}{\tau}N^{BGK}\right]. \tag{5.15}$$

For the MRT case, it is derived similarly with the relaxation time $\frac{1}{\tau}$ being replaced by a diagonal matrix S. Therefore, for the MRT case we have [45]

$$M^{MRT} = A^{-1}\left[I - M^{-1}SMN^{BGK}\right]. \tag{5.16}$$

5.2 Theoretical Modes

The linear stability analysis of the Navier-Stokes equations is largely detailed in [67]. We will here give the main steps behind the procedure. Stability analysis is mainly concerned with analyzing how a wave solution is propagated by the scheme. The Navier-Stokes equations describe the behavior of a fluid and are derived from the principles of mass, momentum, and energy conservation. In two-dimensions, they are expressed as

$$\frac{\partial \rho}{\partial t} + \frac{\partial \rho u_i}{\partial x_j} = 0, \tag{5.17}$$

$$\frac{\partial \rho u_i}{\partial t} + u_j\frac{\partial \rho u_i}{\partial x_j} = -\frac{\partial p}{\partial x_i} + \frac{\partial \tau_{ij}}{\partial x_j}, \tag{5.18}$$

and

$$\frac{\partial \rho e}{\partial t} + \frac{\partial \rho e u_i}{\partial x_i} = -\frac{\partial q_i}{\partial x_i} - p\frac{\partial u_i}{\partial x_i} + \tau_{ij}\frac{\partial u_i}{\partial x_j}. \tag{5.19}$$

The stability analysis starts by linearizing the Navier-Stokes equations. Variables as the sum of a mean value and a small perturbation as

$$u = \bar{u} + u', \tag{5.20}$$

$$\rho = \bar{\rho} + \rho', \tag{5.21}$$

and

$$p = \bar{p} + p'. \tag{5.22}$$

Substituting these expressions into the equations and simplifying, we arrive at the linear Navier-Stokes equations:

$$\frac{\partial U'}{\partial t} + M_1 \frac{\partial U'}{\partial x_1} + M_2 \frac{\partial U'}{\partial x_2} + M_3 \frac{\partial U'}{\partial x_3} = 0, \tag{5.23}$$

where M_1, M_2 and M_3 are matrices defined in [67]. Once linearized, the Navier Stokes equations admit a plane wave solution,

$$U' = \begin{pmatrix} \widehat{p'} \\ \bar{\rho}\widehat{u'} \\ \bar{\rho}\widehat{v'} \\ \bar{\rho}\widehat{w'} \\ \widehat{p'} \end{pmatrix} e^{i(kx-\omega t)}. \tag{5.24}$$

In this equation, the perturbations amplitudes $\widehat{p'}$,$\bar{\rho}\widehat{u'}, \bar{\rho}\widehat{v'}, \bar{\rho}\widehat{w'}$, and $\widehat{p'}$ are complex and should not be amplified for stability. Replacing U' by this value in equation (5.22) yields an eigenvalue problem [67]:

$$\omega U' = M^{NS} U', \tag{5.25}$$

where $M^{NS} = k_1 M_1 + k_2 M_2 + k_3 M_3$. The eigenvalues can be calculated analytically as:

$$\begin{cases} \omega_1 = k \cdot u_0 - i\,|k|^2\,\lambda + |k|\,c_0\sqrt{1-\left(\frac{|k|N}{c_0}\right)^2} \\ \omega_2 = k \cdot u_0 - i\,|k|^2\,\lambda - |k|\,c_0\sqrt{1-\left(\frac{|k|N}{c_0}\right)^2} \\ \omega_3 = k \cdot u_0 - i\,|k|^2\,\nu \\ \omega_3 = \omega_4 \\ \omega_5 = k \cdot u_0 \end{cases}. \tag{5.26}$$

These eigenvalues correspond to the theoretical hydrodynamic modes and are given as dispersion relations. Any propagating in the flow can be expressed as a linear combination of these modes, and the previous expressions link the frequency of the waves to their wavenumbers. These modes can be divided into two acoustic modes, one shear mode, and one entropy mode. The modes ω_1 and ω_2 are known as "acoustic modes" due to the presence of the speed of sound c_0 in their expression. Their propagation speed is $c^{\pm} = k \cdot u_0 \pm |k|\,c_0\sqrt{1-\left(\frac{|k|N}{c_0}\right)^2}$ and these are dissipated as $-|k|^2\,\lambda$. The modes ω_3 and ω_4 are known as the shear mode due to the occurring of the shear stress ν in their expression. They are dissipated as $-i\,|k|^2\,\nu$ and propagated with a speed of $c^s = k \cdot u_0$. Finally, the mode ω_5 is the entropy mode [67].

The previous equations become, ignoring the entropy mode that is considered as a passive scalar due to the isothermal assumption:

$$\begin{cases} \omega^{\pm} = |k|\,(|u_0|\,cos\,(\phi) \pm c_0) - i\,|k|^2\left(\frac{D-1}{D}\nu + \frac{\mu_B}{2}\right) \\ \omega^s = |k|\,|u_0|\,cos\,(\phi) - i\,|k|^2\,\nu \end{cases}, \tag{5.27}$$

With $\omega^{\pm}$ the acoustic modes and ω^s the shear mode. Also, ν is the shear viscosity and μ_B the bulk viscosity. These modes also correspond to those of the LBE-BGK scheme. We also introduce a new parameter, ϕ, to express the angle between the direction of the flow velocity u_0 and the perturbation vector expressed through its wavenumber k in spherical coordinates as follows [68]:

Geometrically, it can be deducted that the spherical coordinates are related to cartesian coordinates via

$$\phi = tan^{-1}\frac{y}{x}, \tag{5.28}$$

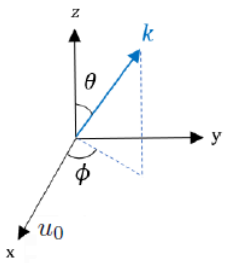

Figure 5.1: Spherical coordinates for the perturbation vector k.

and

$$\theta = cos^{-1}\frac{z}{|\mathbf{k}|}. \tag{5.29}$$

In the following analysis, ϕ is set as $0°$ while θ is set to $\frac{\pi}{2} = 90°$. In other words, we investigate the propagation behavior of waves moving along the x-axis ($i.e\ k = k_x$).

5.3 Linear Stability Analysis: MRT with SF-7 Filter

Dispersive and dissipative errors are respectively related to the propagation speed of each wave in the solution and the damping of the amplitudes of the waves. Ideally, waves should be convected in the domain by the numerical scheme without dispersion or loss of amplitude. This is particularly critical in aeroacoustics simulations, where the solution is dependent on the correct modelling of the acoustic waves. In some cases, though, dissipation is desirable and artificial dissipation can be added as an extra term in the governing equations in order to stabilize the solution. In the following section, the von Neumann Analysis will be applied on the MRT formulation with an applied SF-7 scheme, and results plotted along with the BGK values. The main objective of the analysis is to determine the dissipative and dispersive properties of the scheme and its stability. Analysis was performed for the D2Q9 two-dimensional stencil. The von Neumann Analysis conducted on the MRT scheme with the SF-7 explicit filter yields the following amplification matrices,

$$M^{\bar{f}_i} = (1 - \sigma f)\, A^{-1} \left[I - M^{-1} S M N^{BGK} \right], \tag{5.30}$$

$$M^{\bar{m}_i} = A^{-1}\left[I - M^{-1}SM(I - (1-\sigma f)\,F^{eq})\right], \tag{5.31}$$

and

$$M^{\bar{coll}} = A^{-1}\left[I - M^{-1}SM(1-\sigma f)\,N^{BGK}\right], \tag{5.32}$$

with $M^{\bar{f}_i}, M^{\bar{m}_i}$ and $M^{\bar{coll}}$ respectively the amplification matrices of the MRT scheme with filtered distribution functions, filtered macroscopic variables, and filtered collision operator.

The calculation of these matrices' eigenvalues was performed with the solver *Mathematica* (*i.e.* version 12). Nine eigenvalues were obtained for the D2Q9. Only three are hydrodynamics modes with a physical meaning: the two acoustic modes and the shear modes. The other eigenvalues are kinetic modes that are unphysical. The von Neumann analysis was performed for the three filtering strategies of the MRT, *i.e.* fully filtered LBM, filtered macroscopic variables and filtered collision operator. The analysis is based on the work of Ricot *et al.* [45] and M. Chavez-Modena *et al.* [55, 68]. These strategies will be compared in terms of the kinematic and bulk viscosities, streaming angle ϕ, and Mach number.

To study the effect of the kinematic and bulk viscosities, these were first fixed to the same value. Subsequently, the bulk viscosity is modified via a change of the relaxation times and its effect on the acoustic mode propagation analyzed. The Mach number is defined as

$$Ma = \frac{|u_0|}{c_s}. \tag{5.33}$$

In this expression, u_0 is the streaming velocity defined as u_0=[0.2,0,0], while c_s is the speed of sound. Two Mach Numbers were studied: $Ma = 0$ and $Ma = 0.2$.

In the case of equal shear and bulk viscosities, the relaxation times of Lallemand and Luo [66] were used.

5.3.1 Case with ν=μ_B =$10^{-3}\frac{kg}{ms}$

The bulk and shear viscosities were first fixed to $10^{-3}\frac{kg}{ms}$, which corresponds to values of $s_3 = s_4 = s_5 = 1.988$ in the relaxation time matrix of the MRT collision operators. Lallemand and Luo [66] proposed some values for s_6, s_7 and s_8. In a first step, these were fixed to the

proposed values. Therefore, the diagonal matrix of relaxation time for the MRT operator was

$$S_1 = diag(0, 0, 0, 1.988, 1.988, 1.988, 1.9, 1.9, 1.54). \tag{5.34}$$

The following figure shows the dispersion of the MRT for the three filtering strategies at two different Mach numbers (0 and 0.2) using the relaxation times of matrix S_1. Theoretical values are also plotted.

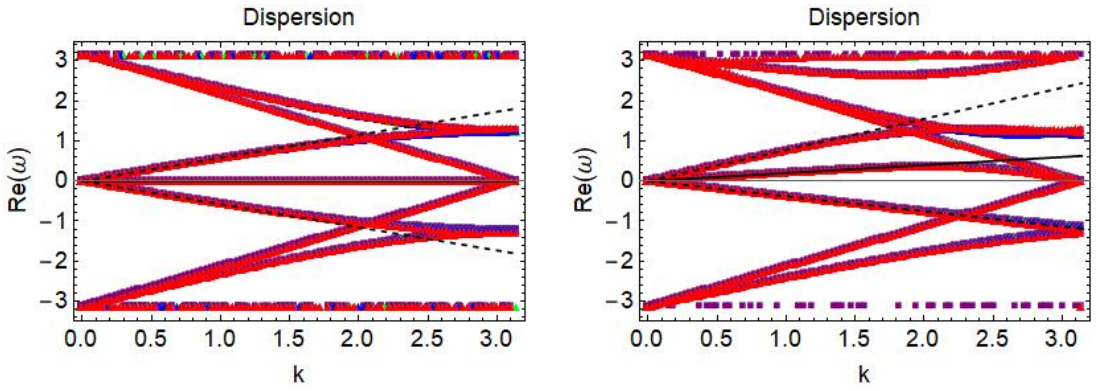

(a) **(b)**

Figure 5.2: Dispersive properties of MRT with different filtering strategies for the same bulk and kinematic viscosities at two different Mach numbers; (a): 0 and (b): 0.2. ■: BGK, ▲: fully filtered LBE, ▲: filtered macroscopic quantities, ▲: filtered collision operator.

The dispersion relation is not affected by the choice of the filter. The dispersive curves for the different filters are almost perfectly superimposed. This is expected, as the filters are constructed symmetrically in order to avoid the introduction of any dispersive errors. At low wavenumbers, the curves of the numerical dispersion and the theoretical one match well. Starting from wavenumbers of $k = 1.7$ approximately, the dispersion error increases, and the numerical results start to depart from their theoretical counterparts. In figure 5.2b, the asymmetry of the curves with respect to the x-axis is in fact due to velocity $u_0 = 0.2$. This asymmetry is not present in figure 5.2a. The dissipation of the shear and acoustic modes is shown in figure 5.3. The shear and the negative and positive modes are identified. We notice that the theoretical shear and acoustic mode overlap. This is expected as the

bulk and kinematic viscosities are the same. We also notice that the shear and acoustic mode behave independently in the MRT case. This is consistent with the fact that, for the MRT, the Chapman-Enskog expansion procedure yields independent shear and bulk viscosities. Compared to the BGK approach, the MRT approach causes a higher dissipation of kinetic modes at higher wavenumbers, which tends to stabilize the solution. Indeed, the MRT approach enables one to relax all the different modes at different rates, hence the kinetic modes that don't have any physical meaning can be more efficiently damped. The BGK solution is plotted in purple. In comparison with the BGK, the filtered MRT approaches yield higher dissipation rates, with the fully filtered LBE approach having the highest dissipation rates. The three filtering approaches lead to different behaviors of the shear and the acoustic modes for both Mach numbers. For a Mach number of 0, the acoustic modes overlap which is not the case at Mach of 0.2. At a Mach of 0.2, the wave propagation velocity is the vector sum of the speed of sound and the flow velocity. This may be observed at wavenumbers greater than $k = 2.0$ when the two curves are differentiated.

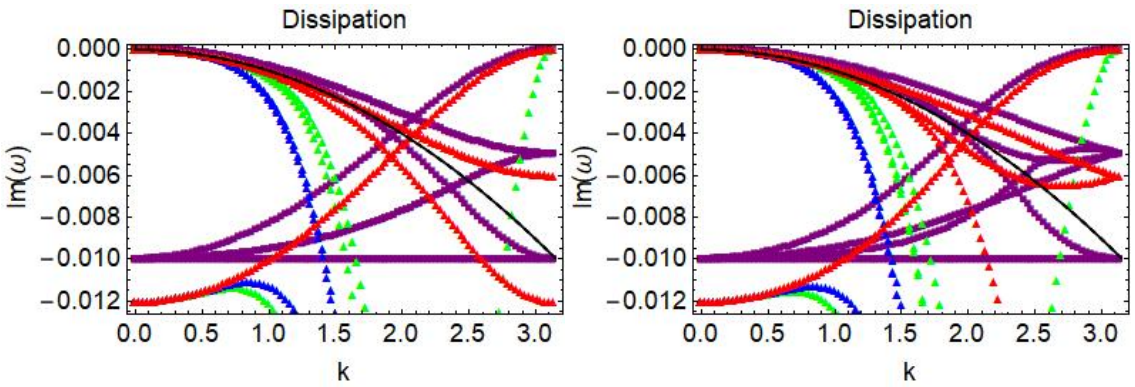

Figure 5.3: Dissipative properties of MRT with different filtering strategies for the same bulk and kinematic viscosities at two different Mach numbers; (a): 0 and (b): 0.2. ■: BGK, ▲: fully filtered LBE, ▲: filtered macroscopic quantities, ▲: filtered collision operator.

Figure 5.4 shows the stability of the three MRT filtering approaches for a Mach number of 0 and a Mach number of 0.2. Recall that the stability condition is given by: $|\lambda| \leq 1$. In other words, perturbations should not be amplified from one time step to another. Observing

the curves, we see that the stability condition is satisfied for all three filtering approaches.

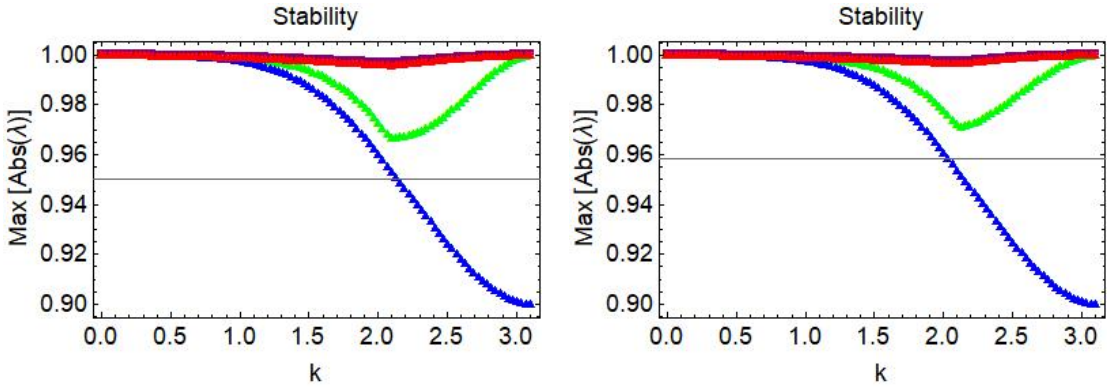

(a) **(b)**

Figure 5.4: Stability properties of MRT with different filtering strategies for the same bulk and kinematic viscosities at two different Mach numbers ((a): 0 and (b): 0.2) (■: BGK, ▲: fully filtered LBE, ▲: filtered macroscopic quantities, ▲: filtered collision operator).

In conclusion the dispersive behavior is not affected by the choice of the scheme. The mean stream velocity, when the Mach number is increased to 0.2, leads to an asymmetry of the dispersion curves and a separation of the acoustic and shear modes in the dissipation plots. This is particularly visible when the MRT is used with the filtered macroscopic quantities approach.

5.3.2 Effect of the Propagation angle θ

We will know keep the same relaxation times S_1 and set a Mach number of 0.2. The von Neumann analysis will be conducted for two angles, $\theta = 0°$ and $\theta = 38°$. The dispersion figures are given in figure 5.5.

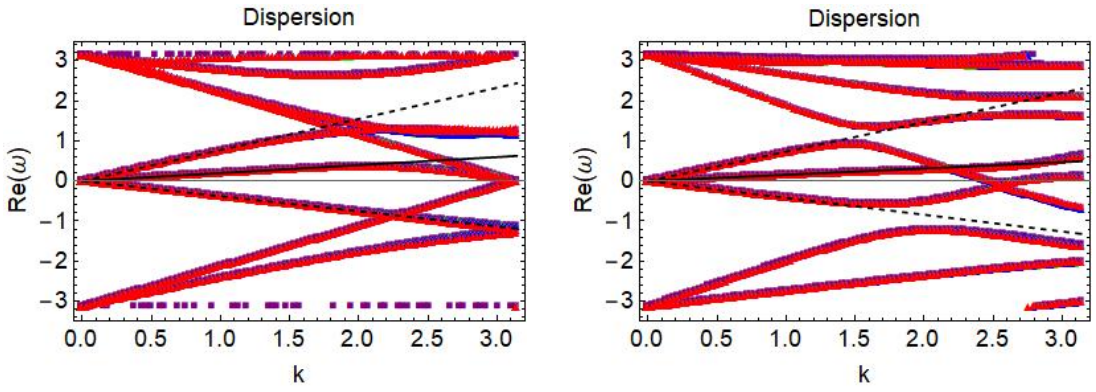

(a) **(b)**

Figure 5.5: Dispersive properties of MRT with different filtering strategies for the same bulk and kinematic viscosities at two different propagation angles θ; (a): 0° and (b): 38°. ■: BGK, ▲: fully filtered LBE, ▲: filtered macroscopic quantities, ▲: filtered collision operator.

As before, the streaming Mach number of 0.2 causes an asymmetry in the figures. As the streaming angle is increased, the numerical curves drift away sooner from the theoretical ones, with a more obvious change. The propagation angle thus yields a greater dispersion error at higher wavenumbers (*i.e.* $k \geq 1.5$)

The dissipation curves are shown in figure 5.6 below. As the streaming angle is increased, some instabilities occur, with positive dissipation around $k = 0.8$ for some modes. For the other modes, the fully filtered LBE approach yields higher dissipation rates at higher wavenumbers, with a cutoff around $k = 2$.

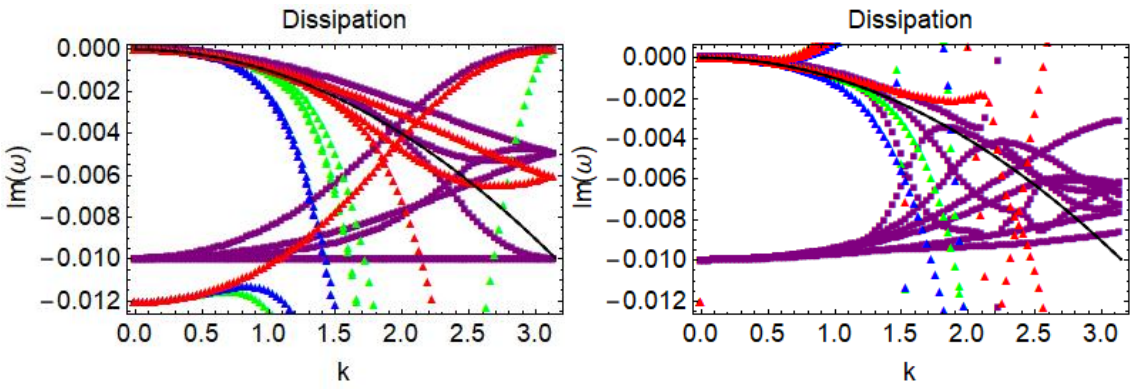

(a) **(b)**

Figure 5.6: Dissipative properties of MRT with different filtering strategies for the same bulk and kinematic viscosities at two different propagation angles θ; (a): 0° and (b): 38°. ■: BGK, ▲: fully filtered LBE, ▲: filtered macroscopic quantities, ▲: filtered collision operator.

Regarding stability (figure 5.7), the Von Neumann stability condition is satisfied for all filtering approaches for $\theta = 0°$. As the streaming angle is increased to $\theta = 38°$, the Von Neumann stability condition $|\lambda| \leq 1$ is violated for all filtering strategies starting from a wavenumber of about $k = 1$. For the fully filtered and filtered collision operator approaches become stable again around a wavenumber of $k = 1.8$. The filtered macroscopic variables approach is unstable for most wavenumbers above $k = 1$ and so should be avoided.

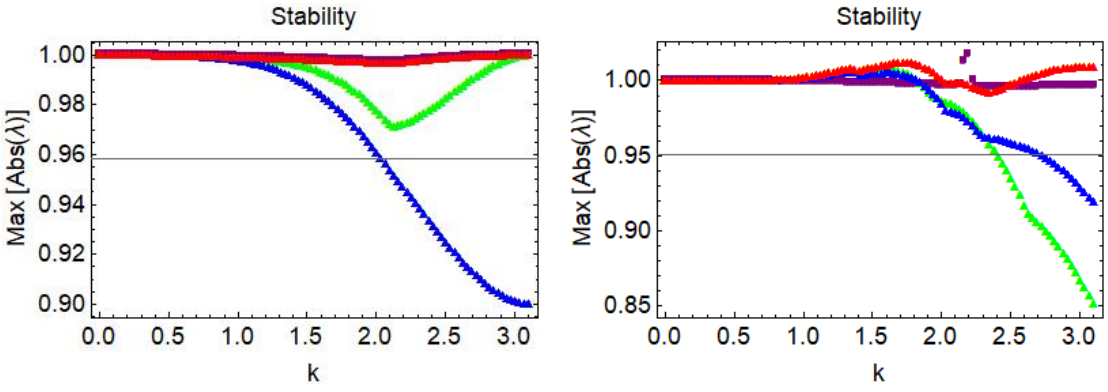

(a) **(b)**

Figure 5.7: Stability properties of MRT with different filtering strategies for the same bulk and kinematic viscosities at two different propagation angles θ; (a): 0° and (b): 38°. ■: BGK, ▲: fully filtered LBE, ▲: filtered macroscopic quantities, ▲: filtered collision operator.

In conclusion, an increase of the propagation to 38° results in a greater dispersion error at higher wavenumbers, $k \geq 1.5$, and the appearance of some instable modes starting from $k = 0.8$, with some positive dissipation.

5.3.3 Case with $\mu_B = 3.66 * 10^{-2}$ kg/ms

Both Dellar [69] and Lallemand and Luo [66] have suggested that increasing the value of the bulk viscosity leads to enhanced LBM stability. In their work, Lallemand and Luo [66] set the bulk viscosity to $3.66 * 10^{-2} \frac{kg}{ms}$ which corresponds to setting s_3 as 1.64 instead of 1.988 previously. The new relaxation time matrix is then given as

$$S_2 = diag(0, 0, 0, 1.64, 1.988, 1.988, 1.9, 1.9, 1.54). \tag{5.35}$$

We will know compare results with S_1 and S_2 at a Mach number of Ma=0.2.

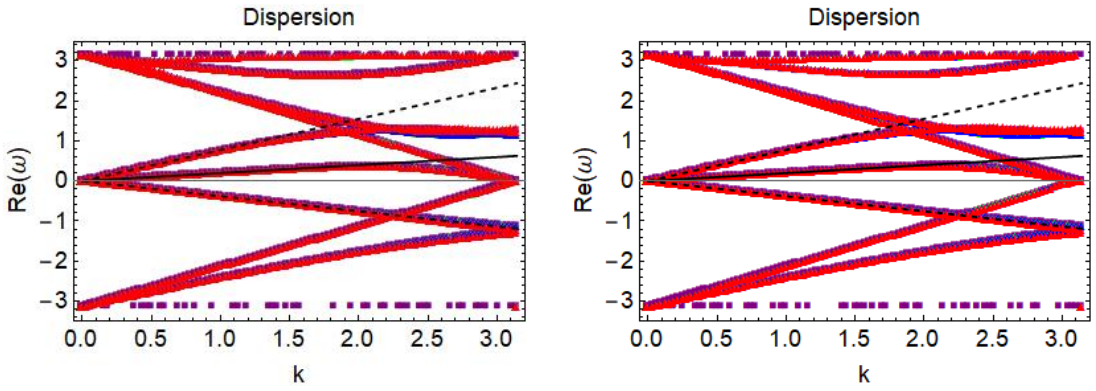

(a) **(b)**

Figure 5.8: Dispersive properties of MRT with different filtering strategies for different bulk and kinematic viscosities; (a): S_1 and (b): S_2. ■: BGK, ▲: fully filtered LBE, ▲: filtered macroscopic quantities, ▲: filtered collision operator.

The streaming velocity is responsible for asymmetry of the two graphs (figure 5.8) with respect to the x-axis. Also, an increase in bulk viscosity (5.8b) does not seem to affect the dispersive properties. This was also reported by [55]. The effects of the bulk viscosity on dissipation can be seen in figure 5.9.

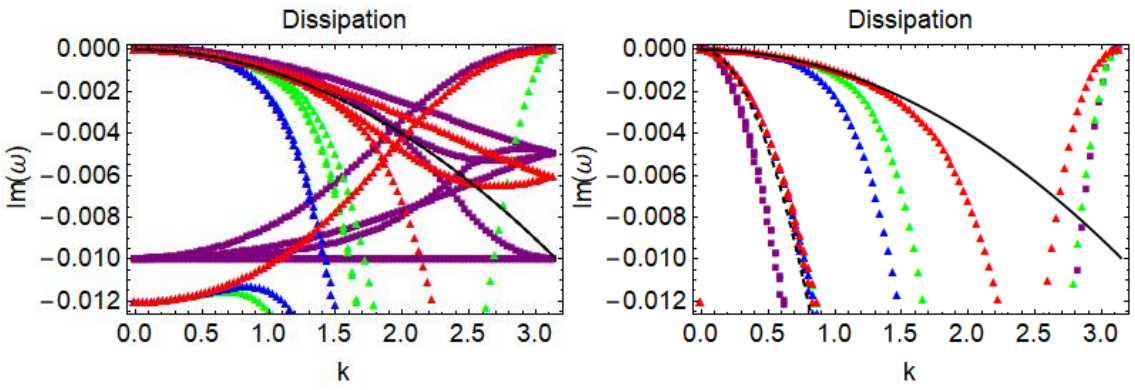

(a) **(b)**

Figure 5.9: Dissipative properties of MRT with different filtering strategies for different bulk and kinematic viscosities; (a): S_1 and (b): S_2. ■: BGK, ▲: fully filtered LBE, ▲: filtered macroscopic quantities, ▲: filtered collision operator.

As expected, an increase in bulk viscosity leads to enhanced dissipation of the modes. This is particularly visible for the BGK. On the left, the curves for all the MRT filtering strategies can be seen superimposed on the theoretical curve. Regarding stability, an increase in bulk viscosity does not seem to affect the Von Neumann stability condition which is satisfied in both cases for the BGK and all the filtering strategies.

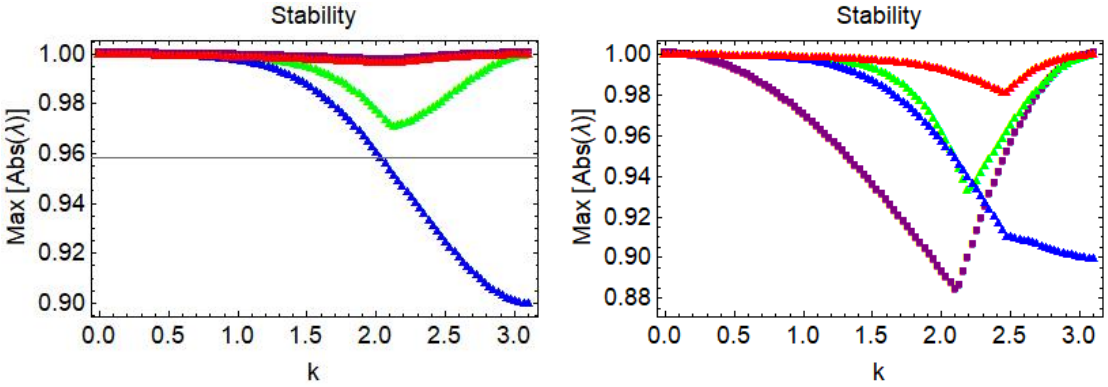

(a) **(b)**

Figure 5.10: Stability properties of MRT with different filtering strategies for different bulk and kinematic viscosities; (a): S_1 and (b): S_2. ■: BGK, ▲: fully filtered LBE, ▲: filtered macroscopic quantities, ▲: filtered collision operator.

To sum up, an increase of the bulk viscosity does not affect the dispersive properties, but leads to greater mode dissipation, as also reported in [55]. It also does not lead to a violation of the Von Neumann stability condition which is still ensured.

5.4 Linear Stability Analysis: BGK with ADM-based Filter

The Von Neumann analysis of the LBM-BGK formulation with the ADM-based filter introduced in Chapter 4 will now be conducted. The chosen filter coefficients are summarized in table 5.1. As a reminder, parameters β_i are obtained by solving a system of equations, and setting $\beta_1 = 1$ (*i.e.* this is described in section 4.4).

β_i	α_i/β_i	α_i
1	1	1
$-2/3$	1.1	$-\frac{22}{30}$
2	1.05	$\frac{21}{10}$
$-2/3$	1.1	$-\frac{22}{30}$

Table 5.1: BGK ADM Von Neumann Analysis filter parameters - Set 1.

Building up from section 5.4, the neighboring points coefficients for each point i are obtained by summing the $n_{i,j}$ and $m_{i,j}$ values over each neighboring cell in a clockwise fashion, starting from node 1 (*i.e.* the top right cell is shown in figure 4.1). The coefficients obtained for the M and N matrices are shown in table 5.2.

Matrix	Central Point	Side Points	Diagonal Points
M	1.05555556	0.48888889	0.24722222
N	1	0.5	0.25

Table 5.2: Filter Coefficients for the M and N matrices - Set 1.

The central point is (i, j). The side points are defined as $(i+1, j), (i, j+1), (i-1, j)$, and (i, j-1). The diagonal points are given as $(i+1, j+1), (i-1, j+1), (i-1, j-1)$, and $(i+1, j-1)$.

The amplification matrix of the LBM-BGK with the SF-7 explicit filter is given as [45]

$$M^{\bar{coll}} = A^{-1}\left[I - \frac{(1-\sigma f)}{\tau} N^{BGK}\right], \tag{5.36}$$

with f the filter function. In what follows, the function $1-\sigma f$ is replaced by a function of the form $\frac{Num}{Den}$, with the numerator Num holding the neighboring coefficients of the M matrix and the denominator Den the neighbors coefficients of the N matrix.

5.4.1 Effect of the Mach number

In what follows the propagation angle θ will be kept to a constant value of $\theta = 0°$. The bulk viscosity is set to $\nu = 10^{-3}\frac{kg}{ms}$, which corresponds to a relaxation time of $\tau = 0.503$. As the bulk and kinematic viscosities are similar in the BGK case, we have $\mu_\nu = 10^{-3}\frac{kg}{ms}$. The following figure shows the dispersive properties of the BGK scheme with the ADM-based filter at a propagation angle of 0° for two different Mach numbers. Also plotted on the figures are the dispersive properties of the BGK and MRT formulations without filtering.

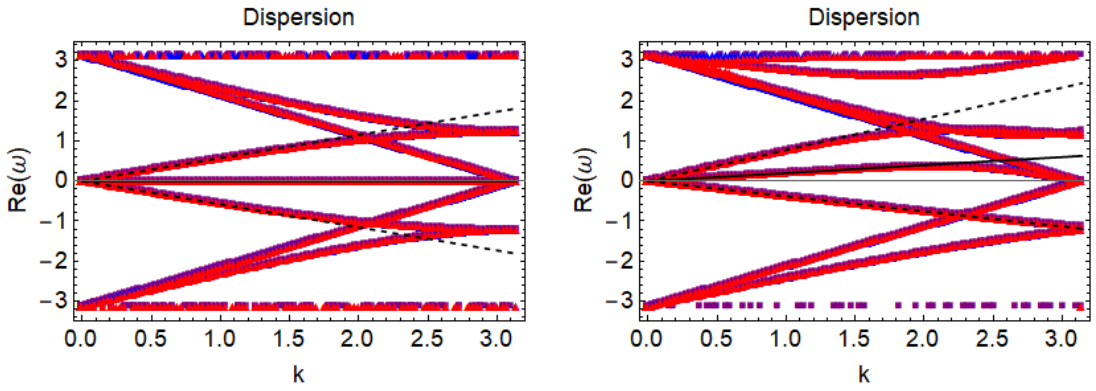

(a) **(b)**

Figure 5.11: Dispersive properties of the LBM-BGK with an ADM-based filter at two different Mach numbers; (a): $Ma = 0$ and (b): $Ma = 0.2$. ■: BGK, ▲: MRT, ▲: filtered BGK.

As before, the dispersion curves are symmetrical with respect to the y-axis and are not affected by the scheme at a Mach number of 0 (5.11a). At low wavenumbers the dispersion error is negligible. Starting from $k = 2$, it becomes more visible. When the Mach number is increased to 0.2 (*i.e.* figure 5.11b), the streaming velocity leads to an assymetry of the plots with respect to the y-axis, seen at wavenumbers higher than $k = 2$. The dissipation plots are shown in figure 5.12. The modes of interest are the shear, and the two acoustic modes, which are superimposed for the MRT case at a Mach number of 0 (5.12a). The LBM-BGK scheme is more dissipative than the BGK and MRT for some modes as seen immediately above $k = 1.5$, while some higher wavenumber modes are less dissipated, as seen above $k = 2.5$ for both Mach numbers.

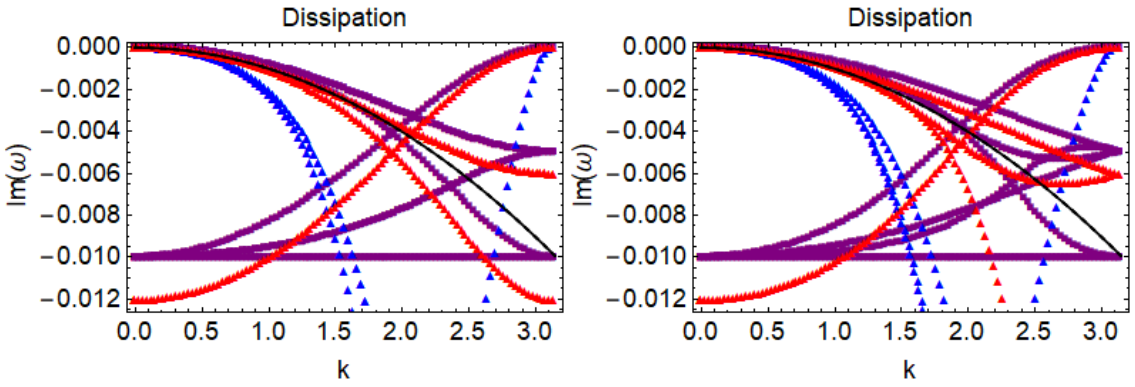

(a) **(b)**

Figure 5.12: Dissipative properties of the LBM-BGK with an ADM-based filter at two different Mach numbers; (a): $Ma = 0$ and (b): $Ma = 0.2$. ■: BGK, ▲: MRT, ▲: filtered BGK.

Stability properties are shown in figure 5.13.

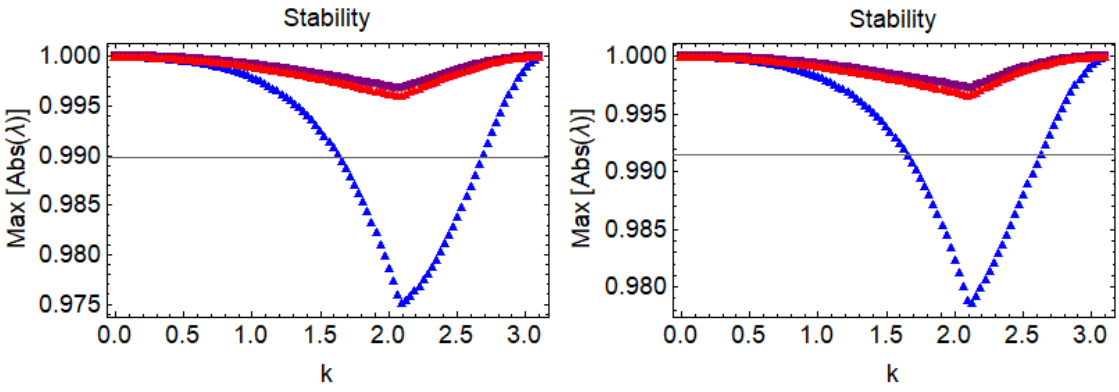

(a) **(b)**

Figure 5.13: Dissipative properties of the LBM-BGK with an ADM-based filter at two different Mach numbers; (a): $Ma = 0$ and (b): $Ma = 0.2$. ■: BGK, ▲: MRT, ▲: filtered BGK.

5.4.2 Effect of the Propagation angle θ

The effect of the propagation angle θ will now be investigated at a streaming Mach number of 0.2. Two angles will be studied: $\theta = 0°$ and $\theta = 38°$. As seen on figure 5.14a, the streaming Mach number leads once again to an assymetry of the dispersion curves with respect to the x-axis. When the propagation angle is increased, as shown in figure 5.14b, the dispersion curves start to deviate sooner from the theoretical values, for an increased dispersive error at higher wavenumbers which can be clearly seen starting from $k = 1.5$. Now regarding dissipation, as shown in figure 5.15, some positive dissipation can be seen for the LBM-MRT as the propagation angle is increased. The dissipative properties of the LBM-BGK with the ADM filter on the other hand are not significantly affected (*i.e.* figure 5.15b).

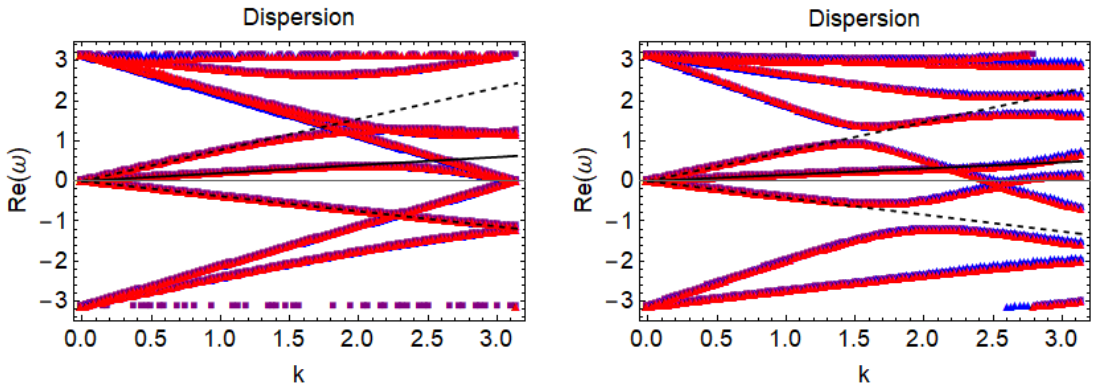

(a) **(b)**

Figure 5.14: Dispersive properties of the LBM-BGK with an ADM-based filter at two different propagation angles; (a): $\theta = 0°$ and (b): $\theta = 38°$. ■: BGK, ▲: MRT, ▲: filtered BGK.

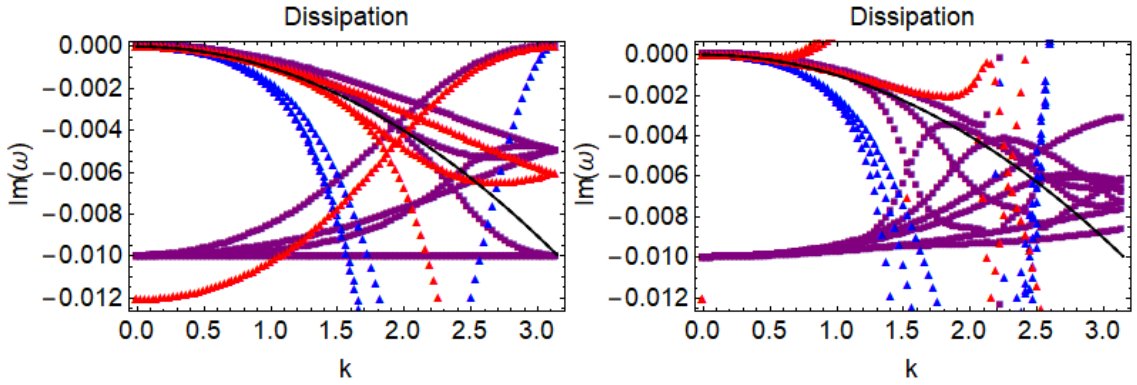

(a) **(b)**

Figure 5.15: Dissipative properties of the LBM-BGK with an ADM-based filter at two different propagation angles; (a): $\theta = 0°$ and (b): $\theta = 38°$. ■: BGK, ▲: MRT, ▲: filtered BGK.

Finally, regarding stability, as the propagation angle is increased, the Von Neumann stability condition ($|\lambda| < 1$) is violated for the MRT and filtered BGK formulations starting from $k = 1.0$ to $k = 2.2$, and starting from $k = 2.3$ again, implying amplification of most wavenumbers. For the filtered BGK, instabilities start from $k = 2.5$, with higher wavenumbers being amplified.

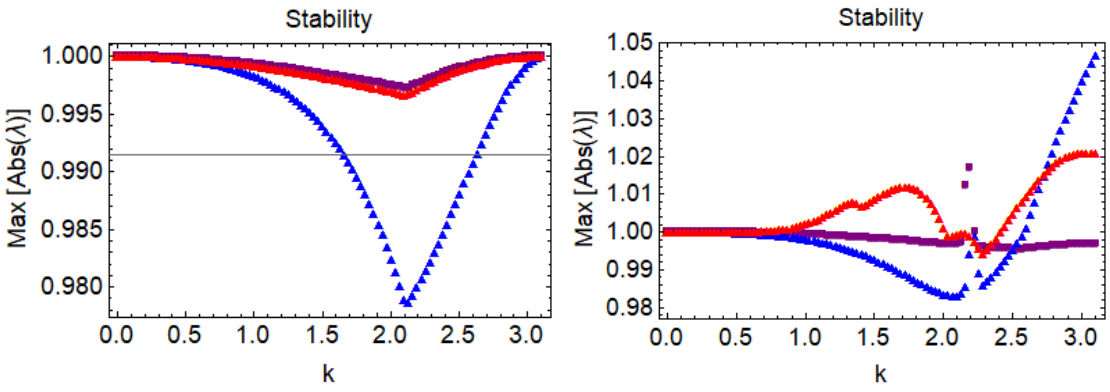

(a) **(b)**

Figure 5.16: Dissipative properties of the LBM-BGK with an ADM-based filter at two different propagation angles; (a): $\theta = 0°$ and (b): $\theta = 38°$. ■: BGK, ▲: MRT, ▲: filtered BGK.

In summary, the dispersive properties are not affected by the choice of scheme but depend on the streaming velocity and angle. The schemes are all stable for a propagation angle of 0° but, at a propagation angle of 38°, instabilities occur for most of the wavenumbers range for the MRT, and at high wavenumbers for the ADM filtered BGK; with a violation of the stability condition.

Chapter 6

Numerical Simulations

In this section, the newly developed schemes (MRT-SF-7 filter and MRT-ADM filter) are compared with other existing schemes. Stability among the different schemes is then compared. In particular, the following schemes are compared: BGK, BGK with SF7 filter, MRT-RM, MRT-RM with filter and BGK with ADM explicit filter.

6.1 Dual Shear Layer

The double shear layer test case consists of two initial shear layers which roll-up due to a Kelvin-Helmholtz instability excited by an O(δ) perturbation in u_y. At poor resolutions, spurious vortices appear in the solution. Minion and Brown [70] showed that these spurious vortices are in fact caused by spurious high wavenumber modes in the solution, linked to grid scale oscillations. The goal is then to analyze how efficient the schemes are at dissipating these high wavenumber oscillations. The second chosen test case, the Taylor Green Vortex, is an often used 3D benchmark test to investigate the effects of turbulence models. The solution starts as a laminar state, with vortex stretching, before these break down, leading to a fully turbulent state. Tracking the evolution of the kinetic energy dissipation rate gives important information about the behavior of the flow and the numerical scheme.

6.1.1 Set Up

The double periodic shear layer case is run on a square domain of dimensions (NxN), with N being the resolution of the domain along the x and y directions. Four grid sizes were used: (32x32), (64x64), (128x128) and finally (256x256). The boundary conditions are periodic and the initial conditions are given by

$$\rho = \rho_0, \tag{6.1}$$

$$u_x = U_0 tanh[w(y/N - 1/4)], y \leq N/2, \tag{6.2}$$

$$u_y = U_0 \delta sin[2\pi(x/N + 1/4)], \tag{6.3}$$

and

$$u_z = \quad U_0 tanh[w(3/4 - y/N)], y \geq N/2, \tag{6.4}$$

where ρ_0 is the reference density which is fixed to 1. The constants w and δ are related respectively to the initial width of the shear layer and the magnitude of the initial perturbation. These are set to

$$w = 80, \tag{6.5}$$

and

$$\delta = 0.05. \tag{6.6}$$

The simulated Reynolds number is $Re = 30,000$ while the Mach number is set to $Ma = 0.2$. The characteristic lattice velocity U_0 can then be computed from the Mach number Ma and the lattice speeds of sound $\left(c_s = \frac{1}{\sqrt{3}}\right)$ as

$$U_0 = Ma * c_s. \tag{6.7}$$

The initial horizontal (u_x) and vertical (u_y) component of the velocity field are shown in figure 6.1.

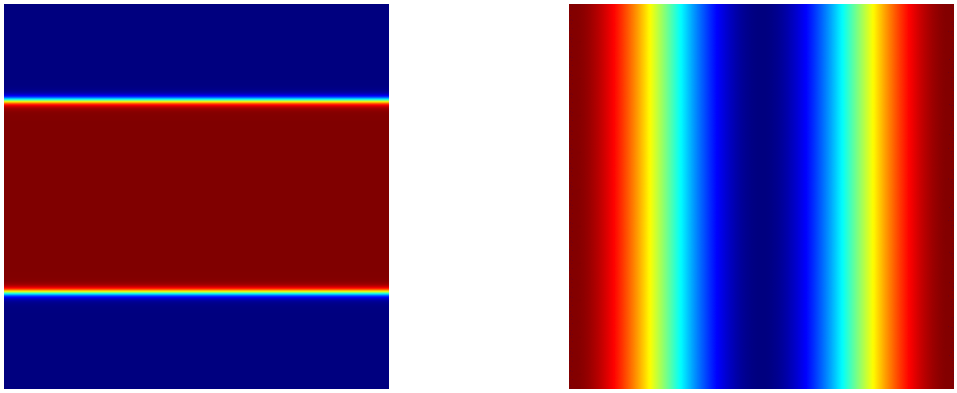

(a) **(b)**

Figure 6.1: Initial horizontal and vertical velocity fields for the dual shear layer case; (a):u_x and (b):u_y.

6.1.2 Grid Sensitivity Study

For all simulations, the physical simulated time is $t = 2t_c$, with the characteristic time t_c being defined as: $t_c = N/U_0$. The isocontours of the vorticity are taken at time t=1 and appear on figure 6.2 at $t/t_c = 1$ on figure 6.2. Note that simulations performed with the LBM-BGK ADM-based filtering approach, at a resolution of $N = 16$, showed significant instabilities. Thus simulations at higher resolutions are not included in what follows for the LBM-BGK ADM-based filter.

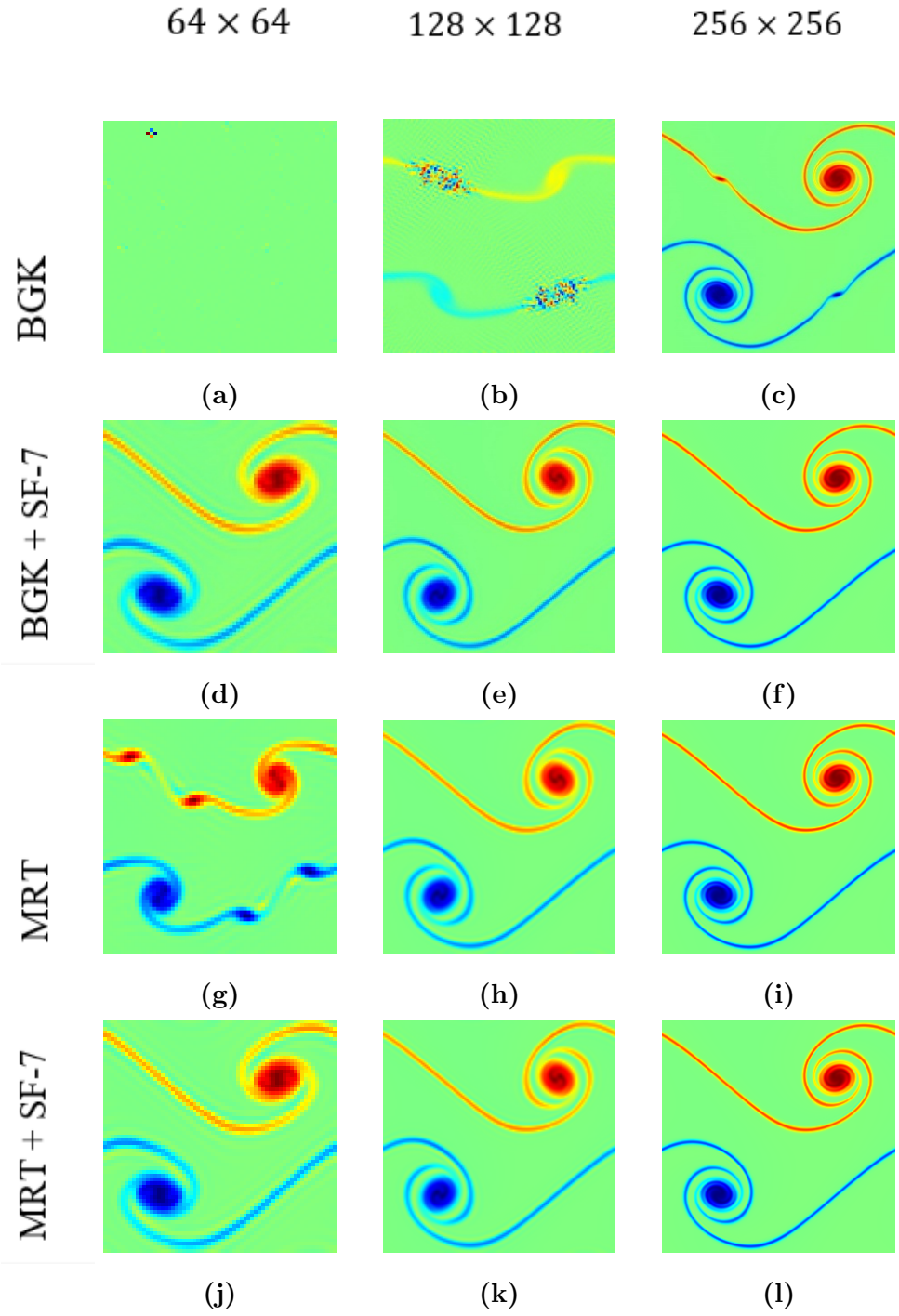

Figure 6.2: Vorticity isocontours at $t/t_c = 1$ ((a): BGK, N=64, (b): BGK, N=128, (b): BGK, N=256, (d): BGK SF-7, N=64, (e): BGK SF-7, N=128, (f): BGK SF-7, N=256, (g): MRT, N=64, (H): MRT, N=128, (i): MRT, N=256, (j): MRT SF-7, N=64, (k): MRT SF-7, N=128, (l): MRT SF-7, N=256).

It is worth nothing that, for grid sizes $N = 32, 64$, and 128, the BGK shows some instabilities. At the highest grid size, $N = 256$, spurious vortices appear. These correspond to extra unphysical modes which appear in the solution. These are thus considered as numerical artefacts. The application of the SF-7 filter in conjunction with the BGK scheme removes these spurious vortices; the simulations are stable for all wavenumbers. At under-resolved simulations, the MRT scheme also exhibits these spurious vortices. Increasing the resolution removes these artefacts, and the correct behavior is recovered at $N = 128$ and $N = 256$. Finally, the application of the SF-7 explicit filter in conjunction with the MRT removes the spurious vortices even as under-resolved grid sizes (*i.e.* $N = 64$). For $N = 128$ and $N = 256$, both the filtered and unfiltered MRT scheme yield similar results.

The dimensionless mean kinetic energy and mean enstrophy are given on figures 6.3 and 6.4.

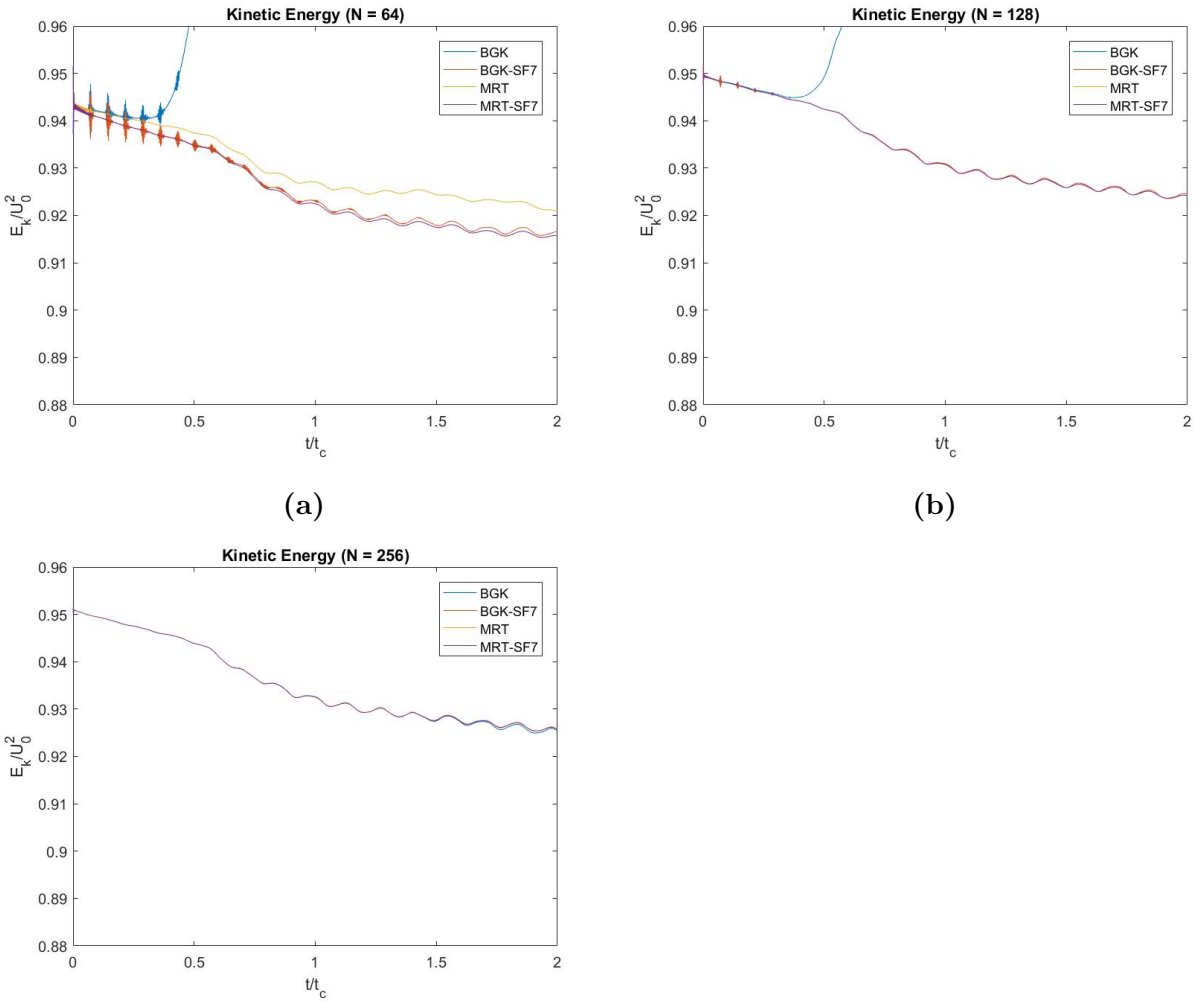

Figure 6.3: Dimensionless Mean Kinetic Energy; (a):$N = 64$, (b):$N = 128$, (c):$N = 256$.

For the under-resolved simulation ($N = 64$), the BGK results deviate early on from the other schemes with amplitudes growing unbounded. For the three other schemes, some wavepacket-like oscillations with a decreasing amplitude and a fixed frequency can be seen until $t/t_c = 1.3$. These oscillations gradually disappear as the grid size is increased; for a fine grid size of $N = 256$, they have disappeared. At a grid size $N = 128$, the BGK scheme still yields unstable results. The three other schemes follow a similar pattern. At the finest grid size (*i.e.* $N = 256$), all schemes yield similar results, with curves that are almost perfectly superimposed. Some negligible deviation can be seen between $t/t_c = 1$ and $t/t_c = 2$ for the BGK case, but the scheme still perfectly follows the trend. For all grid

sizes, starting from $t/t_c = 0.5$, regular oscillations are noticeable in the kinetic energy. As the LBM captures some compressibility, this can be explained by a periodic energy transfer between potential energy and kinetic energy due to compressibility. The enstrophy results are shown in figure 6.4. For the enstrophy, similar observations can be made for the BGK case at the under-resolved simulation ($N = 64$). Results deviate away from the correct trend and quickly reach extremely high values. At $N = 64$, all the approached exhibit wavepacket like oscillations with a decreasing amplitude up until $t/tc = 0.5$ approximately for the BGK and SF-7 and MRT and SF-7 approaches. The enstrophy level are then overpredicted by the MRT without filter while the BGK and SF-7 and MRT and SF-7 approaches yield similar trends. For $N = 128$, the MRT and MRT and SF-7 curves are overlapped and yield very satisfactory results. The BGK and SF-7 approach follows the trend very closely with relatively negligible difference. As before, the BGK yields results which drift away from the correct solution early on. Also, the wavepacket-like oscillations visible in the under-resolved simulation (*i.e.* $N = 64$) have decreased in amplitude. As for the resolution of $N = 256$, all approaches yield satisfactory and very close results. Until $t/t_c = 0.6$, all curves overlap. Some differences can be noticed afterwards, with the BGK overpredicting the enstrophy levels. This is expected as, due to the fact that the BGK used a single relaxation time for all distributions, some discrepancies can occur with the exact results.

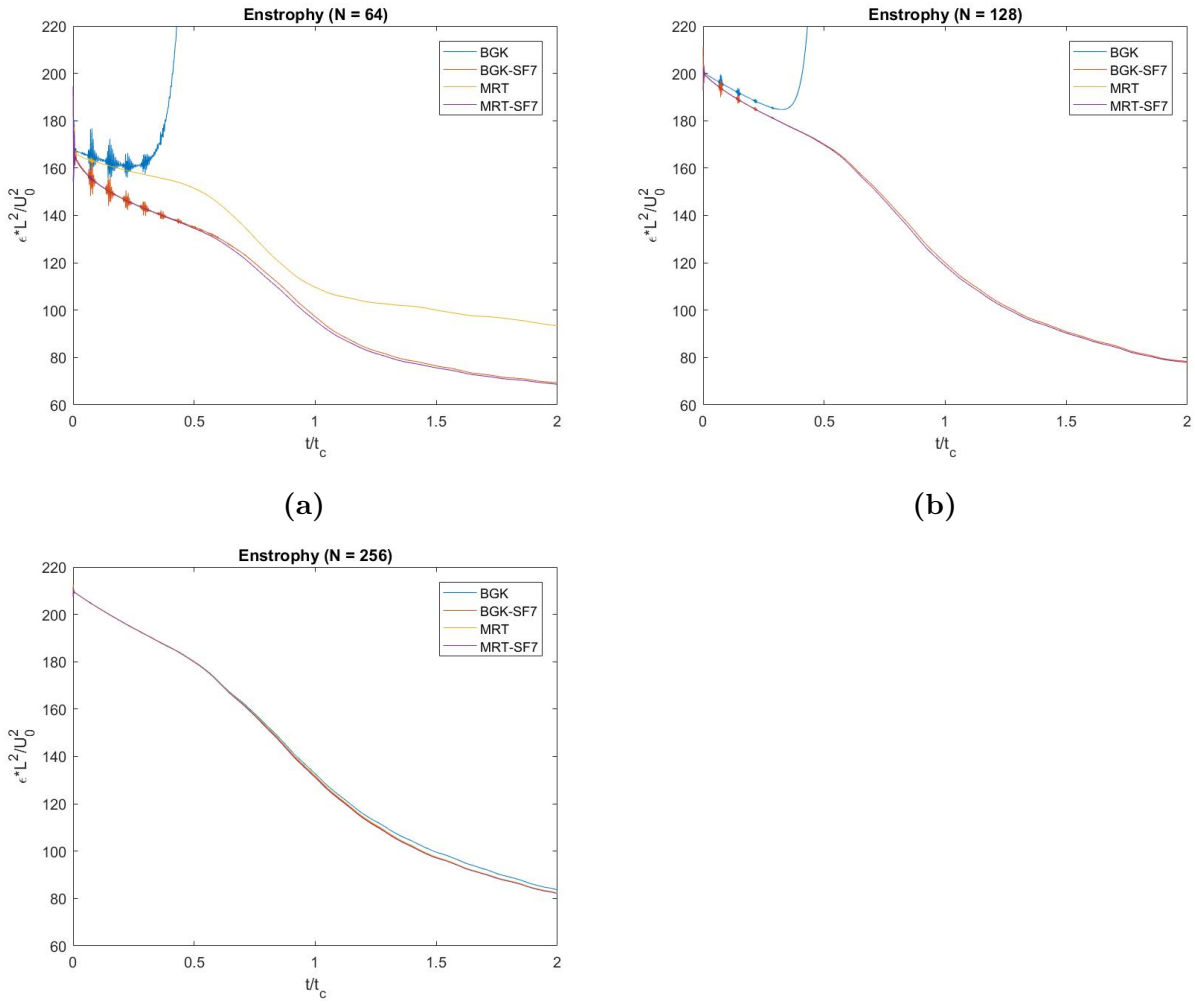

Figure 6.4: Dimensionless Mean Enstrophy; (a):$N = 64$, (b):$N = 128$, (c):$N = 256$.

6.2 Taylor Green Vortex

The second benchmark test chosen is the decaying Taylor Green Vortex (TGV) case. This three-dimensional case is relevant in the analysis of flow transition to turbulence and therefore, is often used to analyze the effect of various schemes and turbulence models in the LBM context. Parameters of interest include vortex stretching as well as small-eddies production and evolution that can be tracked. In this section, the TGV case is conducted with a D3Q19 lattice scheme. Three grid resolutions have been selected for the analysis; two

under-resolved grids ($N = 32$ and $N = 64$) as well as $N = 128$ and $N = 256$. Results are plotted and compared with a TGV DNS case with $N = 512$.

6.2.1 Setup

The initial conditions were chosen based on those specified by the organizers of the AIAA First International Workshop on High Order Methods in Computational Fluid Dynamics [71]. The domain is a 3D cube with length defined as

$$-\pi L \leq x, y, z \leq \pi L. \tag{6.8}$$

Periodic boundary conditions are applied. The initial conditions are set as

$$\begin{cases} u_x = U_0 sin(x/L)cos(y/L)cos(z/L) \\ u_y = -U_0 cos(x/L)sin(y/L) \\ u_z = 0 \\ p_0 = \frac{\rho_0 {U_0}^2}{16}\left[cos(2x/L) + cos(2y/L)\right]\left[cos\left(2z/L\right) + 2\right] \end{cases} \tag{6.9}$$

The reference density, ρ_0, and the reference length, L, are set to one. The reference velocity U_0 can be obtained from the Mach number which is set to $Ma = \frac{U_0}{c_s} = 0.1$. Finally, the kinematic shear viscosity is linked to the Reynolds number: $Re = U_0 L/\nu$.

6.2.2 Grid Sensitivity Study

As previously stated, four collision operators are compared: BGK, BGK with SF-7 filter, MRT, and MRT with SF-7 filter. Three grid sizes are selected: $N = 32$ and $N = 64$ for the under-resolved simulations, and $N = 128$. Each simulation is computed for a physical time of $t = 20t_c$, with t_c the characteristic time defined as $t_c = L/U_0$. The evolution of the kinetic energy and the kinetic energy dissipation rate will be analyzed and compared. The TGV case is characterized by three main steps. The flow is initially laminar with vortex tubes that stretch until they break down around $t/t_c = 5$. The dissipation rate then increases until the peak is reached around $t/t_c = 9$, which corresponds to a fully turbulent state. Kolmogorov's theory [1] explains the energy spectrum as follows: energy is transferred from large to small

scales via an energy cascade, and is dissipated by the smallest eddies in the form of heat. The decay after the peak corresponds to a state of isentropic and homogeneous turbulence [68]. The following figure shows the variations of the vorticity contours throughout time for the BGK collision operator at a grid size $N = 256$ and a reference DNS solution at $N = 512$, shown in black [**?**]. Slices of the vorticity contours (taken at z=0) are presented at a time $t/t_c = 4, 8, 10$ and 16.

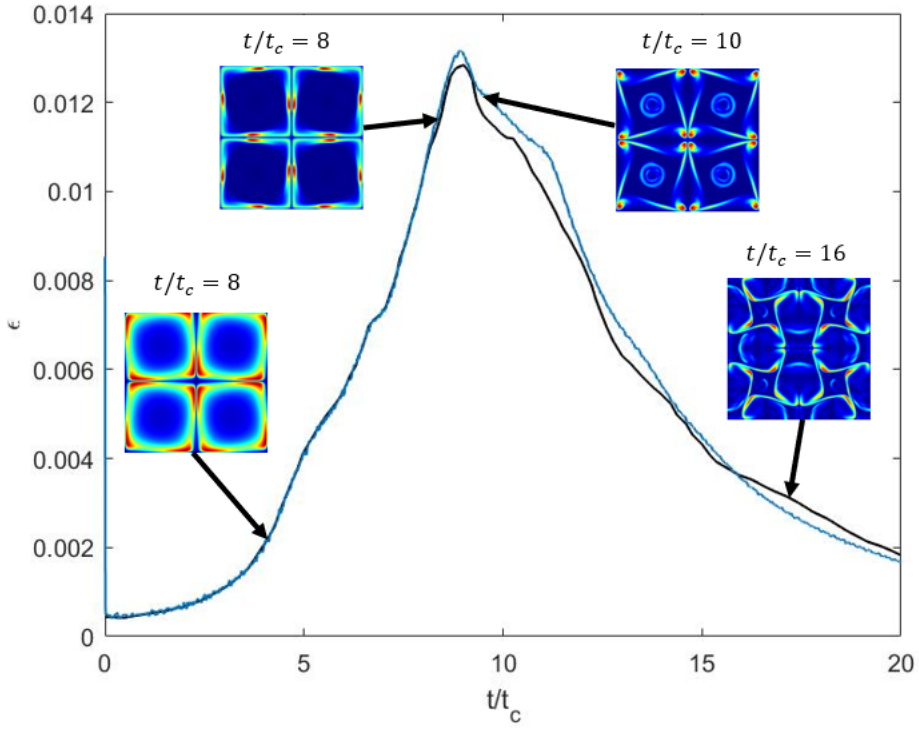

Figure 6.5: Vorticity contours at t/t_c = 4,8,10 and 16 (the DNS results are presented in black while the BGK results are in blue).

The time evolution of the kinetic energy for three grid sizes is plotted for the four schemes (BGK, BGK and SF-7 filter, MRT, and MRT and SF-7 filter) in figures 6.6 and 6.7. As previously stated, four grid sizes are simulated: $N = 32$ and $N = 64$ for the under-resolved simulations, $N = 128$ and $N = 256$. Due to large oscillations in the original results, kinetic energy results were filtered five times with the function "smooth" in *Matlab* in order to extract only relevant trends and enable a clearer analysis. The kinetic energy is given by the following formula:

$$E_k = \frac{1}{\rho_0 V} \int \rho \frac{\mathbf{u}^2}{2} dV, \tag{6.10}$$

where ρ_0 is the characteristic density (*i.e.* $\rho_0 = \rho$) and V is the volume of the domain.

We notice that for under-resolved simulations, the BGK scheme drifts away too much from the rest of the results and is deemed unreliable and unstable. Also, for all schemes at $N = 32$ and $N = 64$, we notice some oscillations up until $t/t_c = 5$ before the curves start to smooth. Now, we previously stated that the vortices stretch up until $t/t_c = 5$ before breaking down. The observed oscillations are, therefore, directly linked to this phenomenon. An increase in grid resolution decreases the sensitivity of results, though, and oscillations are barely visible for $N = 128$ and $N = 256$. Finally, at $N = 256$, results are independent of the choice of collision operator or filtering method, and the curves are superimposed. Overall, the filtered MRT and filtered BGK approaches follow similar trends, while the BGK with the Smagorinsky model seems to underestimate kinetic energy levels at under-resolved simulations. On the opposite the MRT scheme overestimates the kinetic energy levels at under-resolved simulations. This is particularly visible at a resolution $N = 32$.

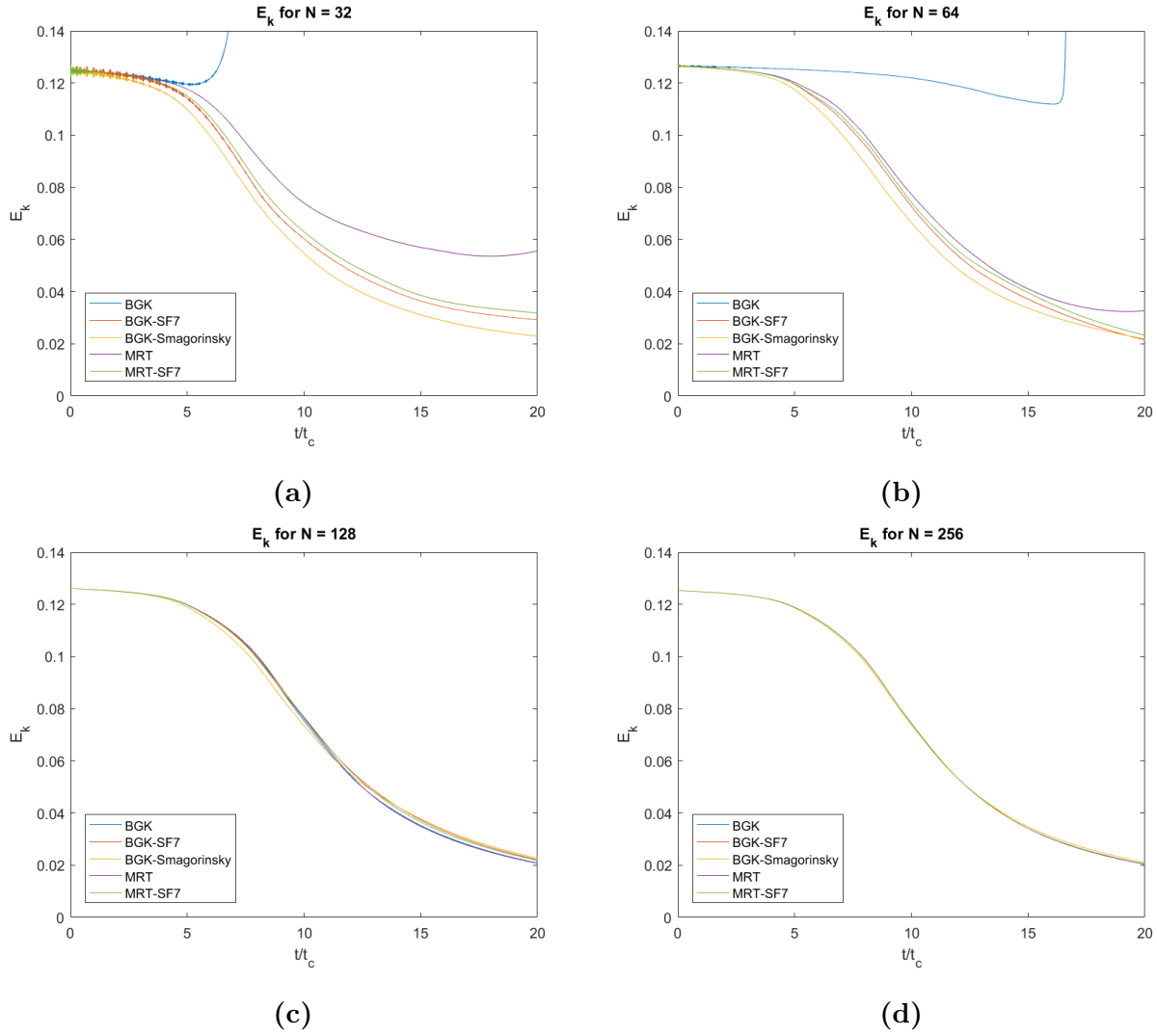

Figure 6.6: Dimensionless Mean Enstrophy; (a):$N = 32$, (b):$N = 64$, (c):$N = 128$, (d):$N = 256$.

To analyze the evolution of the flow in time, the kinetic energy dissipation is computed as

$$\epsilon = -\frac{dE_k}{dt}. \tag{6.11}$$

As before, results are plotted for four schemes and four grid sizes. Also plotted on the figures is the reference solution, obtained via a DNS with $N = 512$ [**?**]. We first notice that the unfiltered BGK scheme yields results completely different from the reference solution for under-resolved simulations (*i.e.* $N = 32$ and $N = 64$). Also, for under-resolved simulations,

the BGK scheme with the SF-7 filter shows many oscillations in the solution, which is also the case the BGK scheme with the Smagorinsky turbulence model. At $N = 32$, the BGK and filter and MRT and filter schemes yield similar trends. However, the MRT scheme with SF-7 filter removes the oscillations present in the solution. The MRT solution has a lower amplitude than the MRT and SF-7 solution. This makes sense, as the explicit filter works by enhancing dissipation in the solution to stabilize it. An interesting observation is that, while the BGK and SF-7, MRT, MRT and SF-7, and BGK-Smagorinsky schemes have a similar evolution of ϵ compared to the reference solution, the increase in the dissipation rate, the peak and the decrease occur earlier than the reference solution. Therefore, the transition occurs earlier and is also faster than the spectral DNS. Concerning the BGK-Smagorinsky scheme, a slight overprediction of the enstrophy can be seen before the peak compared to the filtered BGK and MRT schemes. At a resolution $N = 64$, higher amplitude oscillations can be seen for the BGK and SF-7, MRT and SF-7, and BGK-Smagorinsky cases, but the trends are correctly predicted. Indeed, the transition, peak, and decaying phase occur at the same time as the spectral DNS solution. Some overprediction can however be seen for the BGK-Smagorinsky scheme before the peak. The presence of a turbulence model thus seems to impact how the transition region is predicted. In the laminar region and up until t/t_c, some oscillations can be seen for the MRT case. Here again, the peak is correctly predicted as well as the transition. The decay phase is correctly predicted by the MRT case until $t/t_c = 15$, where excessive dissipation is produced. At $N = 128$, all approaches yield results with oscillations, but the laminar (t/t_c from 0 to 5) and transition phase are accurately captured by all approaches. The peak is correctly captured by both the BGK and MRT approaches, while it is underpredicted by the BGK and SF-7, MRT and SF-7, and BGK-Smagorinsky approaches. Just after the peak, the BGK and MRT approaches overpredict the reference solution while it is the opposite for their filtered counterparts (*i.e.* BGK and SF-7 and MRT and SF-7). Then, starting from $t/t_c = 15$ until the end, all approaches match well with the reference solution. Finally, at $N = 256$, there is a sharp decrease in the oscillations which are almost negligible. All approaches yield overlapping solutions. The transition part is accurately predicted by all schemes which match the reference solution perfectly. However, the peak is overpredicted by all schemes. This overprediction lasts up

until $t/t_c = 15$. Compared to the spectral DNS, the schemes add excessive dissipation. The trends are then swapped after $t/t_c = 15$ until $t/t_c = 20$, with all approaches underpredicting the reference solution.

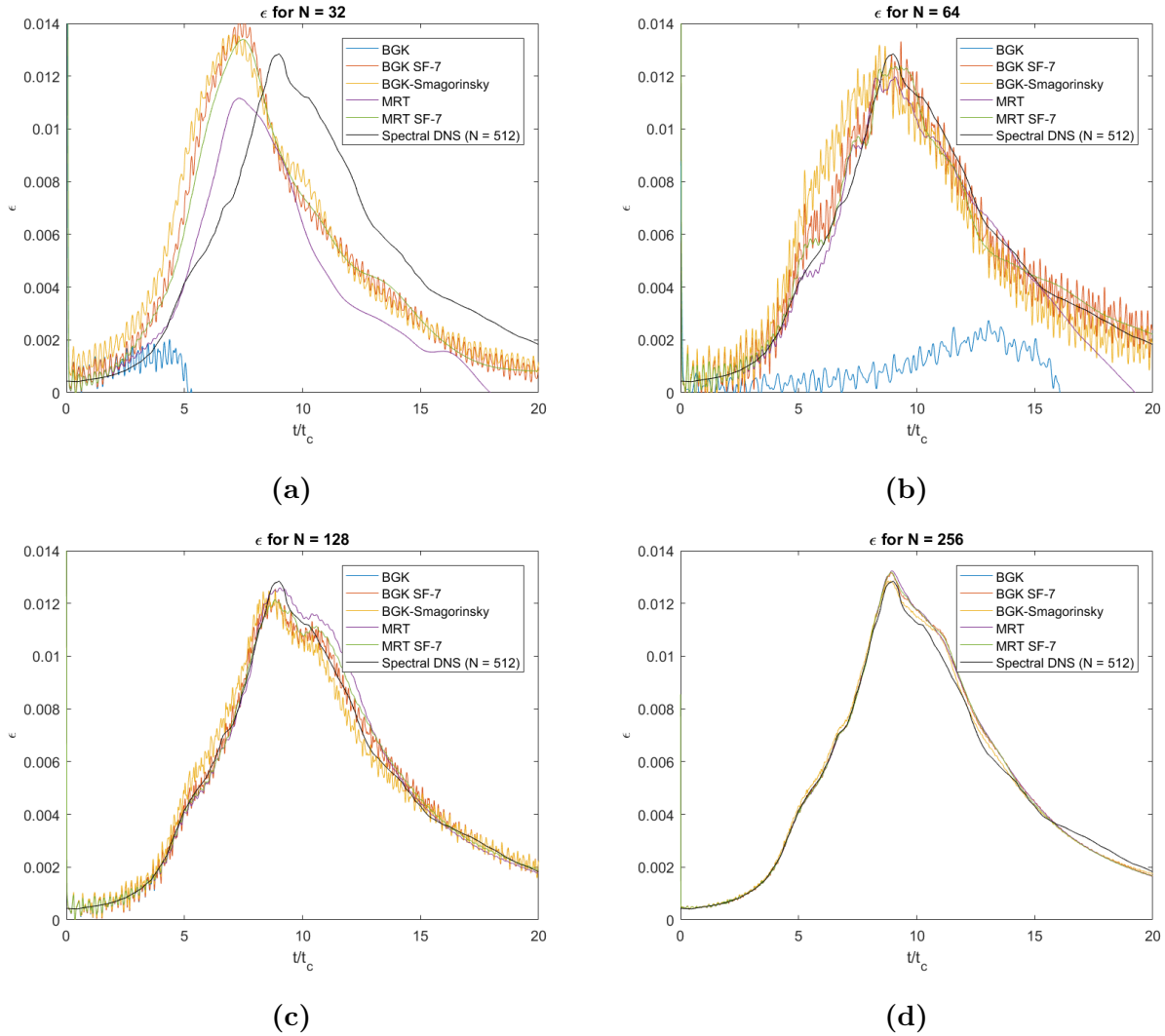

Figure 6.7: Dimensionless Mean Enstrophy; (a):$N = 32$, (b):$N = 64$, (c):$N = 128$, (d):$N = 256$.

Chapter 7

Conclusion

Due to its linearity, ability to deal with complex boundaries due to simple boundary condition, and local behavior which enables parallelisation, the Lattice Boltzmann Method has gathered large and growing interest this past decade in the CFD community, in particular for jet noise simulations. Its most simple formulation, the LBM-SRT, is known for its instabilities at low viscosities and high Reynolds number flows. A Von Neumann analysis conducted in [45] showed how this is caused by the interaction of the acoustic mode with other modes. Alternative formulations can be used, such as the LBM-MRT which introduces multi-relaxation times. During the collision process, each moment can be relaxed towards equilibirum at a different rate, which enhances the stability of the method, but still yields some instabilities for under-resolved simulations. As shown by [45], explicit filtering of the BGK leads to improved stability.

In this work, alternative explicit filtering strategies for stabilization the Lattice Boltzmann method were investigated. A seven-point stencil explicit filter (*i.e* SF-7 [46]) was implemented with the MRT method. A Von Neumann analysis was conducted on the explicit filter with the LBM-MRT formulation, for three different filtering strategies. The dispersive, dissipative, and stability properties were characterized and analyzed. It was shown that while viscosity does not affect the dispersive error, modifying the Mach number affects the disersion error of the shear and acoustic modes. For consistance with [45], filtering was applied on the collision operator.

The filtered MRT operator was then validated with a two-dimensional Dual Shear Layer and a three-dimensional Taylor-Green Vortex test cases. The enhanced performance of the explicitely filtered MRT collision operator in comparison with the unfiltered BGK and MRT schemes was demonstrated for the Dual Shear Layer, with the filtered MRT successfully removing spurious vortices in under-resolved simulations. In three-dimensions, the filtered MRT was compared with the unfiltered BGK and MRT, explicitely filtered BGK, BGK with a Smagorinsky turbulence model, and a reference DNS solution (*i.e* at a resolution of $N = 512$). The scheme was successful in capturing the energy decay trends of the isotropic turbulence, yielding results close to the reference solution. It was also shown to significantly decrease the oscillations present in the solution.

Concerning the implications of this research, these findings are of particular interest in aeroacoustic simulations of jet engines for instance, where a good compromise must be made between computational efficiency and accuracy of the collision operator. In applications involving the MRT, the application of an appropriate filter, as the SF-7 in this case, can thus lead to more accurate results. The Von Neumann analyses are of particular interest to link observed instabilities with the used bulk and kinematic viscosities, propagation angles, and the Mach number. The results from the Von Neumann analyses were able to show for instance that some zones of instabilities are expected as the propagation vector is not aligned anymore with the x-axis. It was also shown that higher wavenumbers are particularly subjected to these instabilities which can result in spurious waves in the solution.

These findings are particularly relevant for aeroacoustics applications, where the accurate resolution of acoustic pressure waves is essential. In such applications, any instabilities in pressure waves oscillations can affect the computed noise levels. Another relevant application, as mentioned in the introduction, is the study of multiphase flows, where interfaces must be handled accurately. Multiphase flows usually include fluids with different viscosities and/or velocities. The use of a stable scheme is then mandatory to avoid instabilities at low resolutions as seen previously in the shear layer case. The use of the LBM-MRT scheme

with an explicit filtering strategy can be more suitable in such cases.

An explicit filter based on ADM methods for LES was also introduced and its stability analysis performed and compared with the unfiltered BGK and MRT schemes. Applying the filter on the collision operator, it was shown that some modes were further dissipated, some higher wavenumber modes were not. The benchmarking of the ADM-based filter in two- and three-dimensions is currently dependant on the optimization of the filter parameters β_i and α_i so that they ensure stability while efficiently filtering the solution. Additionally, the conduction of simulations at resolutions higher than $N = 16$ is currently hampered by computational costs due to the matrix inversion needed at each time step, as seen from equation 4.16.

The first contribution of this thesis was the implementation of an explicit filter on the MRT collision operator (chapter 6). The second and third contributions were the condition of a Von Neumann analysis the LBM-MRT with the SF-7 explicit filter and the LBM-BGK with an ADM-based filter. In both instances the dispersive, dissipative, and stability properties of the operators were analyzed. Finally, the fourth contribution is the benchmarking of the MRT explicit filtering approach with a two-dimensional dual shear layer and a three-dimensional Taylor Green Vortex test cases.

This work has opened many doors for further exploration of certain topics in the future. The first possible study is the optimization of the ADM-based filter coefficients for the BGK collision operator in two-dimensions (D2Q9) and three-dimensions (D3Q19). The second possible study is the optimization the matrix inversion process in the *Palabos* implementation, in order to reduce computational costs for higher resolutions. The third possible study is the benchmarking of the BGK with the ADM-based filter in two dimensions (*i.e* Dual Shear Layer) and three-dimensions (*i.e* Taylor-Green Vortex). The fifth possible future study consists in a linear stability analysis of the ADM-based filter for the D1Q3, D3Q15 and D3Q27 stencils. Finally, the SF-7 explicit filter can be implemented on the BGK and MRT collision operators with non periodic boundary conditions, in both two- and three-dimensions.

Appendix A

Appendix

A.1 Chapman – Enskog Analysis

The goal of the Chapman-Enskog analysis is to relate the distribution functions (f_i) to the Navier-Stokes equations and the macroscopic variables. It is valid for incompressible fluids at a small Mach number. The objective is to derive the Navier-Stokes equations and be able to correlate parameters such as viscosity and relaxation time to the kinematic viscosity of the Navier-Stokes equations. As previously stated, it emerges from the need to separate the various physical phenomena happening at various scales. These scales actually correspond to various orders of the Knudsen number ϵ.Thus, a multiscale expansion is introduced.

A power law series in terms of ϵ, the Knudsen number, for f_i, is first introduced as

$$f_i = {f_i}^{(0)} + \epsilon {f_i}^{(1)} + \epsilon^2 {f_i}^{(2)} + ... \tag{A.1}$$

Power law series for ∂x and ∂t are also introduced as follows,

$$\frac{\partial}{\partial x} = \epsilon \frac{\partial}{\partial x_1}, \tag{A.2}$$

and

$$\frac{\partial}{\partial t} = \epsilon \frac{\partial}{\partial t_1} + \epsilon^2 \frac{\partial}{\partial t_2}. \tag{A.3}$$

Now, conservation laws state that ${f_i}^{eq}$ must satisfy

$$\begin{cases} \sum_i f_i = \sum_i {f_i}^{eq} = \rho \\ \sum_i c_i f_i = \sum_i {f_i}^{eq} = \rho u \end{cases}, \tag{A.4}$$

for respectively the conservation of mass and momentum. It follows that

$$\begin{cases} \sum_i {f_i}^{neq} = 0 \\ \sum_i {f_i}^{neq} = 0 \end{cases}, \tag{A.5}$$

with ${f_i}^{neq} = \epsilon {f_i}^1 + \epsilon^2 {f_i}^2$. We recall that the Lattice Boltzmann Equation is given by, for the BGK scheme,

$$f_i(x + \Delta x, t + \Delta t) - f_i(x, t) = -\frac{1}{\tau} f_i(x, t) - {f_i}^e q(x, t). \tag{A.6}$$

A Taylor series expansion is then performed on the left-hand side, yielding

$$f_i(x + \Delta x, t + \Delta t) = f_i(x, t) + \sum_{n=0}^{\infty} \frac{\epsilon^n}{n!} (\partial_t + e_i \partial_x)^n f_i(x, t). \tag{A.7}$$

Indeed, the parameter ϵ can be taken as Δt and, expanding on time,

$$\implies f_i x + \Delta x, t + \Delta t = f_{ix}, t + \Delta t (\partial_t + c_{ix} \partial_x) f_i + \frac{(\Delta t)^2}{2} (\partial_t + c_{ix} \partial_x)^2 f_i + O[(\Delta t)^3] + ... \tag{A.8}$$

The next step is to replace f_i by its expansion ($f_i = f^0 + \epsilon f^1 + \epsilon^2 f^2 + ...$) as

$$\begin{aligned} &[\Delta t (\epsilon^1 \partial_{t_1} + \epsilon^2 \partial_{t_2} + e_i \epsilon \partial_x)(f^0 + \epsilon f^1 + \epsilon^2 f^2) \\ &+ \frac{(\Delta t)^2}{2} (\epsilon^1 \partial_{t_1} + \epsilon^2 \partial_{t_2} + e_i \epsilon \partial_x)^2 (f^0 + \epsilon f^1 + \epsilon^2 f^2)] \\ &- \frac{1}{\tau} [f^0 + \epsilon f^1 + \epsilon^2 f^2 - f^{eq}]. \end{aligned} \tag{A.9}$$

Terms depending on ϵ^0, ϵ^1 and ϵ^2 are then separated. Let LHS designate the left-hand side and RHS the right-hand side.

Then, for $\epsilon^{\mathbf{0}}$, LHS = 0 (no ε^0 order terms for ∂_t and ∂_x) and RHS = $0 = \frac{1}{\tau} [f^0 - f^{eq}]$. Hence,

$$\implies f^0 = f^{eq}. \tag{A.10}$$

For $\epsilon^{\mathbf{1}}$, LHS $= \left(\partial_t{}^0 + e_i\partial_x\right) f^0$ and RHS $= -\frac{1}{\tau}f^1$. Thus,

$$\implies \Delta t\partial_{t1} + e_i\partial_x f_0 = -\frac{1}{\tau}f^1. \tag{A.11}$$

For $\epsilon^{\mathbf{2}}$, LHS $= \left(\partial_{t_1} + e_i\partial_x\right) f^1 + \partial_{t_2} f^0$ and RHS $= -\frac{1}{\tau}f^2$. Therefore,

$$\implies \Delta t\partial_{t1} + e_i\partial_x f_1 + \Delta t\partial_t{}^2 f_0 + \frac{\Delta_t{}^2}{2}\partial_{t1} + e_i\partial x f_0 = -\frac{1}{\tau}f^2. \tag{A.12}$$

Now, as the terms of the order of ε^2 are sufficient to recover the Navier-Stokes equation, the Lattice Boltzmann Method is considered to be of second order.

A.1.1 Conservation of Mass

Taking the zeroth-order moment of equation (A.11):

$$\sum_i \left(\partial_{t_1} + e_i\partial_x\right) f_i{}^{eq} = \sum_i -\frac{1}{\tau}f_i{}^1 = 0, \tag{A.13}$$

according to (A.5).

$$\Rightarrow \frac{\partial\rho}{\partial t_1} + u_j\frac{\partial\rho}{\partial x_j} = 0, \tag{A.14}$$

using (A.4).

A.1.2 Conservation of Momentum

A similar approach can be followed for the conservation of momentum. The following equation is obtained,

$$\frac{\partial(\rho u_i)}{\partial t} + \frac{\partial(\rho u_i u_j)}{\partial x_j} = -\frac{\partial}{\partial x_i}(\frac{c^2\rho}{3})$$
$$\frac{\partial}{\partial x_j}[(\tau - 0.5)\Delta t(\frac{c^2}{3}\rho(\frac{\partial u_j}{\partial x_i} + \frac{\partial u_i}{\partial x_j}) - \frac{\partial}{\partial x_k}(\rho u_i u_j u_k))]. \tag{A.15}$$

A.2 D2Q9 MRT Matrix construction

To construct the MRT matrix a Gramm-Schmidt orthogonalization procedure can be used. It will be decribed in what follows.

We recall that LBM-MRT equation is given by:

$$f_i(\vec{x} + c\vec{e_i}\Delta t, t + \Delta t) - f_i(x,t) = M^{-1}SM[f_i(x,t) - f_i{}^e q(x,t)], \tag{A.16}$$

with the moments are obtained as: $m_i = Mf_i(\vec{x},t)$ and $M = M(\mathbf{u})$, $\mathbf{u}$ being the reference velocity. The first step is to specify the order of the moments. Let $X = (e_{ix} - u)^m$ and $Y = (e_{iy} - u)^n$ represent the difference between the microscopic and the reference velocities [68]. Following Geier *et al.* [72], the nine non-orthogonal moment basis vectors using the monomials X and Y are

$$M(\mathbf{u}) = \begin{pmatrix} X^0Y^0 \\ X \\ Y \\ X^2 + Y^2 \\ X^2 - Y^2 \\ XY \\ X^2Y \\ XY^2 \\ X^2Y^2 \end{pmatrix} \tag{A.17}$$

Applying the Gramm-Schmidt orthogonalization procedure, the matrix $M(\mathbf{u})$ is obtained [68],

$$M(\mathbf{u}) = \begin{pmatrix} X^0Y^0 \\ X \\ Y \\ 3(X^2+Y^2)-4 \\ X^2-Y^2 \\ XY \\ 3X(X^2+Y^2)-5 \\ 3Y(X^2+Y^2)-5 \\ (9/2)(X^2+Y^2)^2-(21/2)(X^2+Y^2)+4 \end{pmatrix} \tag{A.18}$$

This is re-expressed as

$$M(\mathbf{u}) = \begin{pmatrix} \rho \\ j_x \\ j_y \\ e \\ p_{xx} \\ p_{xy} \\ q_x \\ q_y \\ \epsilon \end{pmatrix}. \tag{A.19}$$

Moments can be ordered as follows,

Moment	Order	Description
ρ	0^{th}	Density
j_x	1^{st}	x-momentum
j_y	1^{st}	y-momentum
e	2^{nd}	Kinetic energy
p_{xx}	2^{nd}	x-symmetric traceless viscous stress tensor
p_{xy}	2^{nd}	y-symmetric traceless viscous stress tensor
q_x	3^{rd}	x-energy flux
q_y	3^{rd}	y-energy flux
ε	4^{th}	Related to the kinetic energy square

Table A.1: Moments and their description for the D2Q9 case.

$$M(\mathbf{u}) = \begin{pmatrix} m_0 \\ m_1 \\ m_2 \\ m_3 \\ m_4 \\ m_5 \\ m_6 \\ m_7 \\ m_8 \end{pmatrix} = \begin{pmatrix} \rho \\ j_x \\ j_y \\ e \\ p_{xx} \\ p_{xy} \\ q_x \\ q_y \\ \epsilon \end{pmatrix}. \tag{A.20}$$

These moments and their description are summarized in table A.1.

In the two-dimensional case, the resulting matrix for raw moments $M(\mathbf{u} = 0)$ is given by equation A.21 [68].

$$M = \begin{pmatrix} 1 & 1 & 1 & 1 & 1 & 1 & 1 & 1 & 1 \\ 0 & 1 & 0 & -1 & 0 & 1 & -1 & -1 & 1 \\ 0 & 0 & 1 & 0 & -1 & 1 & 1 & -1 & -1 \\ -4 & -1 & -1 & -1 & -1 & 2 & 2 & 2 & 2 \\ 0 & 1 & -1 & 1 & -1 & 0 & 0 & 0 & 0 \\ 0 & 0 & 0 & 0 & 0 & 1 & -1 & 1 & -1 \\ 0 & -2 & 0 & 2 & 0 & 1 & -1 & -1 & 1 \\ 0 & 0 & -2 & 0 & 2 & 1 & 1 & -1 & -1 \\ 4 & -2 & -2 & -2 & -2 & 1 & 1 & 1 & 1 \end{pmatrix} \tag{A.21}$$

A.3 D3Q19 MRT Matrix construction

A new term is introduced in three dimensions, $Z = (e_{iz} - u)^l$ [68]. As proposed by Geier *et. al* [72], the moment sets are given in equation A.22.

$$M(\mathbf{u}) = \begin{pmatrix} X^0Y^0Z^0 \\ X \\ Y \\ Z \\ XY \\ XZ \\ YZ \\ X^2 + Y^2 + Z^2 \\ XY^2 + XZ^2 \\ X^2Y + YZ^2 \\ X^2Z + Y^2Z \\ XY^2 - XZ^2 \\ X^2Y - YZ^2 \\ X^2Z - Y^2Z \\ X^2Y^2 + X^2Z^2 + Y^2Z^2 \\ X^2Y^2 + X^2Z^2 - Y^2Z^2 \\ X^2Y^2 - X^2Z^2 \end{pmatrix}. \tag{A.22}$$

As for the two-dimensional case, applying the Gram-Schmidt orthogonalization procedure to the matrix yields [68]:

$$M(\mathbf{u}) = \begin{pmatrix} X^0Y^0Z^0 \\ X \\ Y \\ Z \\ XY \\ XZ \\ YZ \\ X^2 - Y^2 \\ (X^2 + Y^2 + Z^2) - 3Z^2 \\ (X^2 + Y^2 + Z^2) - 2 \\ 3(XY^2 + XZ^2) - 4X \\ 3(YX^2 + YZ^2) - 4Y \\ 3(ZX^2 + ZY^2) - 4Z \\ (XY^2 - XZ^2) \\ (YX^2 - YZ^2) \\ (ZX^2 - ZY^2) \\ 3(X^2Y^2 + X^2Z^2 - 2Y^2Z^2) - 2(2X^2 - Y^2 - Z^2) \\ 3(X^2Y^2 - X^2Z^2) - 2(Y^2 - Z^2) \\ 3(X^2Y^2 + X^2Z^2 + Y^2Z^2) - 4(X^2 + Y^2 + Z^2) + 4 \end{pmatrix}. \tag{A.23}$$

The corresponding moments are

$$M(\mathbf{u}) = \begin{pmatrix} \rho \\ j_x \\ j_y \\ j_z \\ p_{xy} \\ p_{xz} \\ p_{yz} \\ p_{ww} \\ 3p_{xx} \\ e \\ q_x \\ q_y \\ q_z \\ m_x \\ m_y \\ m_z \\ 3\pi_{xx} \\ \pi_{ww} \\ \epsilon \end{pmatrix}. \tag{A.24}$$

In the above moments, m_x, m_y and m_z are the asymmetric third-order moments, and π is related to the kinetic energy.

In three-dimensions, the resulting transformation matrix of raw moments is [68]

$$M(\mathbf{u}=0)=\begin{pmatrix}
1 & 1 & 1 & 1 & 1 & 1 & 1 & 1 & 1 & 1 & 1 & 1 & 1 & 1 & 1 & 1 & 1 & 1 \\
0 & -1 & 0 & 0 & -1 & -1 & -1 & -1 & 0 & 0 & 1 & 0 & 0 & 1 & 1 & 1 & 1 & 0 & 0 \\
0 & 0 & -1 & 0 & -1 & 1 & 0 & 0 & -1 & -1 & 0 & 1 & 0 & 1 & -1 & 0 & 0 & 1 & 1 \\
0 & 0 & 0 & -1 & 0 & 0 & -1 & 1 & -1 & 1 & 0 & 0 & 1 & 0 & 0 & 1 & -1 & 1 & -1 \\
0 & 0 & 0 & -1 & 0 & 0 & -1 & 1 & -1 & 1 & 0 & 0 & 1 & 0 & 0 & 1 & -1 & 1 & -1 \\
0 & 0 & 0 & 0 & 1 & -1 & 0 & 0 & 0 & 0 & 0 & 0 & 0 & 1 & -1 & 0 & 0 & 0 & 0 \\
0 & 0 & 0 & 0 & 0 & 0 & 1 & -1 & 0 & 0 & 0 & 0 & 0 & 0 & 0 & 1 & -1 & 0 & 0 \\
0 & 0 & 0 & 0 & 0 & 0 & 0 & 0 & 1 & -1 & 0 & 0 & 0 & 0 & 0 & 0 & 0 & 1 & -1 \\
0 & 1 & -1 & 0 & 0 & 0 & 1 & 1 & -1 & -1 & 1 & -1 & 0 & 0 & 0 & 1 & 1 & -1 & -1 \\
0 & 1 & 1 & -2 & 2 & -1 & -1 & -1 & -1 & 1 & 1 & -2 & 2 & 2 & -1 & -1 & -1 & -1 & -1 \\
-2 & -1 & -1 & -1 & 0 & 0 & 0 & 0 & 0 & 0 & -1 & -1 & -1 & 0 & 0 & 0 & 0 & 0 & 0 \\
0 & 4 & 0 & 0 & 1 & 1 & 1 & 1 & 0 & 0 & -4 & 0 & 0 & -1 & -1 & -1 & -1 & 0 & 0 \\
0 & 0 & 4 & 0 & 1 & -1 & 0 & 0 & 1 & 1 & 0 & -4 & 0 & -1 & 1 & 0 & 0 & -1 & -1 \\
0 & 0 & 0 & 4 & 0 & 0 & 1 & -1 & 1 & -1 & 0 & 0 & -4 & 0 & 0 & -1 & 1 & -1 & 1 \\
0 & 0 & 0 & 0 & -1 & -1 & 1 & 1 & 0 & 0 & 0 & 0 & 0 & 1 & 1 & -1 & -1 & 0 & 0 \\
0 & 0 & 0 & 0 & -1 & 1 & 0 & 0 & 1 & 1 & 0 & 0 & 0 & 1 & -1 & 0 & 0 & -1 & -1 \\
0 & 0 & 0 & 0 & 0 & 0 & -1 & 1 & 1 & -1 & 0 & 0 & 0 & 0 & 0 & 1 & -1 & -1 & 1 \\
0 & -4 & 2 & 2 & 1 & 1 & 1 & 1 & -2 & -2 & -4 & 2 & 2 & 1 & 1 & 1 & 1 & -2 & -2 \\
0 & 0 & -2 & 2 & 1 & 1 & -1 & -1 & 0 & 0 & 0 & -2 & 2 & 1 & 1 & -1 & -1 & 0 & 0 \\
4 & 0 & 0 & 0 & -1 & -1 & -1 & -1 & -1 & -1 & 0 & 0 & 0 & -1 & -1 & -1 & -1 & -1 & -1
\end{pmatrix}. \tag{A.25}$$

A.4 Selective Filter Coefficients

	SF-5	SF-7	Tam-5	Bogey-9
d_0	6/16	5/16	0.287392842460	0.243527493120
d_1	-4/16	-15/64	-0.226146951809	-0.204788880640
d_2	1/16	3/32	0.106303578770	0.120007591680
d_3		-1/64	-0.023853048191	-0.045211119360
d_4				0.008228661760

Table A.2: Selective filters coefficients

Bibliography

[1] A. Kolmogorov, "Dissipation of energy in locally isotropic turbulence," *Akademiia Nauk SSSR Doklady*, vol. 16, 1941.

[2] J. Boussinesq, "Essai sur la théorie des eaux courantes," *Mémoires présentés par divers savants à l'Académie des Sciences*, vol. 1, pp. 1–680, 1877.

[3] F. Schmidt, "About boussinesq's turbulent viscosity hypothesis: historical remarks and a direct evaluation of its validity," *Comptes Rendus Mécanique*, vol. 1, pp. 617–627, 2007.

[4] L. Prandtl, "Z. angew," *Math. Mech.*, vol. 5, pp. 136–139, 1925.

[5] A. Johansson, *Engineering Turbulence Models and their Development, with Emphasis on Explicit Algebraic Reynolds Stress Models*. Vienna: Springer, 2002.

[6] W. M. H. Verteeg, *An Introduction to Computational Fluid Dynamics: The Finite Volume Method*. London: Pearson, 2007.

[7] D. Wilcox, "Formulation of the k–ω turbulence model revisited," *AIAA Journal*, vol. 46, pp. 2823–2838, 2008.

[8] P. Spalart and S. Allmaras, "A one-equation turbulence model for aerodynamic flows," *Recherche Aérospatiale*, pp. 5–21, 1994.

[9] P. Spalart, "Trends in turbulence treatments," in *Proceedings of the Fluids 2000 Conference and Exhibit*, (Denver, CO, U.S.A), 06 2000.

[10] Y. Zhiyin, "Large-eddy simulation: Past, present and the future," *Chinese Journal of Aeronautics*, vol. 28, pp. 11–24, 2015.

[11] M. Hamdi, S. Elalimi, and S. Nasrallah, "Large eddy simulation-based lattice boltzmann method with different collision models," in *Exergy for A Better Environment and Improved Sustainability 1. Green Energy and Technology* (I. D. e. F. Aloui, ed.), pp. 661–683, Cham: Springer, 2018.

[12] Y. Koda, "Lattice Boltzmann Method for Simulating Turbulent Flows," Master's thesis, University of Waterloo, Canada, 2013.

[13] J. Hardy, Y. Pomeau, and O. de Pazzis, "Time evolution of a two-dimensional classical lattice system," *Physical Review Letters*, vol. 31, pp. 276–279, 1973.

[14] F. Higuera, S. Succi, and R. Benzi, "Lattice gas dynamics with enhanced collisions," *EPL (Europhysics Letters)*, vol. 9, pp. 345–349, 1989.

[15] S. Harris, *An introduction to the theory of the Boltzmann equation*. Mineola, New York: Dover Publications, Inc, 2004.

[16] Y. Qian, D. D'Humières, and P. Lallemand, "Lattice bgk models for navier-stokes equations," *EPL (Europhysics Letters)*, vol. 17, pp. 479–484, 1992.

[17] H. Chen, S. Chen, and W. Matthaeus, "Recovery of the navier-stokes equations using a lattice-gas boltzmann method," *Physical Review A*, vol. 45, pp. 5339–5342, 1992.

[18] A. Kuzmin, T. Kruger, O. Shardt, G. Silva, E. Viggen, and H. Kusumaatmaja, *The Lattice Boltzmann Method: Principles and Practices*. Basel: Springer International Publishing AG Switzerland, 2017.

[19] J. Li, "Appendix: Chapman-enskog expansion in the lattice boltzmann method," 2015.

[20] P. Lew, L. Mongeau, and A. Lyrintzis, "Noise prediction of a subsonic turbulent round jet using the lattice-boltzmann method," *The Journal of Acoustical Society of America*, vol. 3, pp. 1118–1127, 2010.

[21] H. Gong, "Numerical study of jet noise generated by turbofan engine nozzles equipped with internal forced lobed mixers using the lattice boltzmann method," Master's thesis, McGill University, Canada, 2013.

[22] R. Brionnaud, G. Trapani, M. Modena, and D. Holman, "Direct noise computation with a lattice-boltzmann method and application to industrial test cases," in *Proceedings of the 22nd AIAA/CEAS Aeroacoustics Conference*, (Lyon, France), 05-06 2016.

[23] R. Kotapati, A. Keating, S. Kandasamy, B. Duncan, R. Shock, and H. Chen, "The lattice-boltzmann-vles method for automotive fluid dynamics simulation, a review," in *Proceedings of the SIAT 2009*, 01 2009.

[24] M. Han, R. Ooka, and H. Kikumoto, "Lattice boltzmann method-based large-eddy simulation of indoor isothermal airflow," *International Journal of Heat and Mass Transfer*, vol. 130, pp. 700–709, 03 2020.

[25] J. R. Barraza and R. Deiterding, "Towards a generalised lattice boltzmann method for aerodynamic simulations," *Journal of Computational Science*, vol. 45, p. 101182, 2020.

[26] X. Zhang, "Lattice boltzmann implementation for fluids flow simulation in porous media," *International Journal of Image, Graphics and Signal Processing*, vol. 3, 06 2011.

[27] A. Nabovati and A. Sousa, "Fluid flow simulation in random porous media at pore level using lattice boltzmann method," in *New Trends in Fluid Mechanics Research* (L. J. e. Zhuang F.G., ed.), pp. 518–521, Berlin, Heidelberg: Springer, 2007.

[28] Y. Hu, D. Zuo, Y. Zhang, F. Xu, B. Li, and S. Liang, "Thermal performances of saturated porous soil during freezing process using lattice boltzmann method," *Journal of Thermal Analysis and Calorimetry*, 2019.

[29] C. Ay, C.-W. Young, and C.-F. Young, "Application of lattice boltzmann method to the fluid analysis in a rectangular microchannel," *Computers and Mathematics with Applications*, vol. 64, pp. 1065–1083, 09 2012.

[30] M. Szucki, J. Suchy, J. Lelito, P. Malinowski, and J. Sobczyk, "Application of the lattice boltzmann method for simulation of the mold filling process in the casting industry," *Heat and Mass Transfer*, vol. 53, pp. 3421–3431, 2017.

[31] C. Sun and L. Munn, "Lattice boltzmann simulation of blood flow in digitized vessel networks," *Comput Math Appl.*, vol. 55, pp. 1594–1600, 2008.

[32] M. H.-A. Raheed, *Mesoscopic lattice Boltzmann method for simulating blood flow and red blood cell deformation in microvessels*. PhD thesis, Bangor University, 2012.

[33] M. Vargas and M. Argenta, "A representation of pulsatile blood flow in arteries or veins using lattice boltzmann," *Revista Brasileira de Ensino de Fisica*, vol. 37, pp. 4304–1–4304–12, 2015.

[34] A. Wongcharoen and S. Kingkaew, "Simulation of stenosis in blood vessel by lattice boltzmann method," in *2018 Third International Conference on Engineering Science and Innovative Technology (ESIT)*, pp. 1–4, 2018.

[35] Y. Liu, "A lattice boltzmann model for blood flows," *Applied Mathematical Modelling*, vol. 36, 07 2012.

[36] V. Mengle and W. Dalton, "Lobed mixer design for noise suppression: Vol. 1," Tech. Rep. NASA CR-2002-210823/Vol1, NASA, 2002.

[37] E. Manoha, J. Bulté, and B. Caruelle, "Lagoon: an experimental database for the validation of cfd/caa methods for landing gear noise prediction," in *Proceedings of the 14th AIAA/CEAS Aeroacoustics Conference (29th AIAA Aeroacoustics Conference*, (Vancouver, British Columbia), 05 2008.

[38] E. Manoha, J. Bulté, V. Ciobaca, and B. Caruelle, "Lagoon: Further analysis of aerodynamic experiments and early aeroacoustics results," in *Proceedings of the 15th AIAA/CEAS Aeroacoustics Conference*, (Miami, Florida), 05 2009.

[39] E. Manoha and B. Caruelle, "Summary of the lagoon solutions from the benchmark problems for airframe noise computations-iii workshop," in *Proceedings of the 21st AIAA/CEAS Aeroacoustics Conference*, (Dallas, Texas), 06 2015.

[40] L. Sanders, E. Manoha, S. B. Khelil, and C. Francois, "Lagoon: Cfd/caa coupling for landing gear noise and comparison with experimental database," in *Proceedings of the 17th AIAA/CEAS Aeroacoustics Conference (32nd AIAA Aeroacoustics Conference)*, (Portland, Oregon), pp. 6–8, 2011.

[41] S. Ahmed, G. Ramm, and G. Faltin, "Some salient features of the time-averaged ground vehicle wake," in *SAE Technical Paper*, SAE International, 02 1984.

[42] Y. Hu, D. Zuo, Y. Zhang, F. Xu, B. Li, and S. Liang, "Thermal performances of saturated porous soil during freezing process using lattice boltzmann method," *Journal of Thermal Analysis and Calorimetry*, 2019.

[43] M. Wang, Y. Feng, G. Pande, A. Chan, and W. Zuo, "Numerical modelling of fluid-induced soil erosion in granular filters using a coupled bonded particle lattice boltzmann method," *Computers and Geotechnics*, vol. 82, 02 2017.

[44] F. Gharibi, S. Jafari, M. Rahnama, B. Khalili, and E. J. Javaran, "Simulation of flow in granular porous media using combined lattice boltzmann method and smoothed profile method," *Computers and Fluids*, vol. 177, pp. 1–11, 11 2018.

[45] D. Ricot, S. Marié, P. Sagaut, and C. Bailly, "Lattice boltzmann method with selective viscosity filter," *Journal of Computational Physics*, vol. 228, pp. 4478–4490, 2009.

[46] P. Skordos, "Initial and boundary conditions for the lattice boltzmann method," *Phys. Rev. E*, vol. 48, pp. 4823–4842, 1993.

[47] B. H. U. Frisch and Y. Pomeau, "Lattice-gas automata for the navier-stokes equations," *Physical Review Letters*, vol. 56, pp. 1505–1508, 1986.

[48] G. McNamara and G. Zanetti, "Use of a boltzmann equation to simulate lattice-gas automata," *Physical Review Letters*, vol. 61, pp. 2332–2335, 1988.

[49] F. Higuera and J. Jimenez, "Boltzmann approach to lattice gas simulations," *EPL (Europhysics Letters)*, vol. 9, pp. 663–668, 1989.

[50] P. Bhatnagar, E. Gross, and M. Krook, "A model for collision processes in gases. i. small amplitude processes in charges and neutral one-component systems," *Physics Rev. Lett.*, vol. 94, pp. 511–525, 1954.

[51] Q. Zou and X. He, "On pressure and velocity boundary conditions for the lattice boltzmann bgk model," *Physics of Fluids*, vol. 9, p. 1591–1598, 1997.

[52] Y. Bao and J. Meskas, "Lattice boltzmann method for fluid simulations," tech. rep., Simon Fraser University, 2011.

[53] E. Kam, R. So, and R. Leung, "Lbm simulation of aeroacoustics and non-reflecting boundary conditions," *AIAA Journal*, vol. 45, pp. 1703–1712, 2007.

[54] M. Schlaffer, *Non-reflecting Boundary Conditions for the Lattice Boltzmann Method*. PhD thesis, Technische Universitat Munchen, Germany, 2013.

[55] M. Chavez-Modena, E. Ferrer, and G. Rubio, "Improving the stability of multiple-relaxation lattice boltzmann methods with central moments," *Computers and Fluids*, vol. 172, pp. 397–409, 2018.

[56] O. Vasilyev, T. Lund, and P. Moin, "A general class of commutative filters for les in complex geometry," *Journal of Computational Physics*, vol. 146, pp. 82–104, 1998.

[57] C. Tam, J. Webb, and Z. Dong, "A study of the short wave components in computational acoustics," *Journal of Computational Acoustics*, vol. 1, pp. 1–30, 1993.

[58] C. Bogey and C. Bailly, "A family of low dispersive and low dissipative explicit schemes for flow and noise computations," *Journal of Computational Physics*, vol. 194, pp. 194–214, 2004.

[59] M. Najafiyazdi, *Large-Eddy Simulations on Unstructured Grids using Explicit Differential Filters in Approximtate Deconvolution Models*. PhD thesis, McGill University, Canada, 2019.

[60] M. Germano, "Differential filters for the large eddy numerical simulation of turbulent flows," *The Physics of Fluids*, vol. 1755, 1986.

[61] M. Germano, "Differential filters of elliptic type," *The Physics of Fluids*, vol. 1757, 1986.

[62] A. Najafi-Yazdi, M. Najafi-Yazdi, and L. Mongeau, "A high resolution differential filter for large eddy simulation: Towards explicit filtering on unstructured grids," *Journal of Computational Physics*, vol. 292, pp. 272–286, 2015.

[63] J. Sterling and S. Shen, "Stability analysis of lattice boltzmann methods," *Journal of Computational Physics*, vol. 123, 1996.

[64] G. Wissocq, P. Sagaut, and J.-F. Boussuge, "An extended spectral analysis of the lattice boltzmann method: modal interactions and stability issues," *Journal of Computational Physics*, 2018.

[65] Wolfram, "Wolfram mathematica: Modern technical computing," 2020. `https://www.wolfram.com/mathematica/`, Last accessed on 2020-08-27.

[66] P. Lallemand and L. Luo, "Theory of the lattice boltzmann method: dispersion, dissipation, isotorpy, galilean invariance and stability," *Physical Review E*, vol. 61, pp. 6546–6562, 2000.

[67] S. Marié, *Etude de la méthode Boltzmann sur Réseau pour les simulations en aéroacoustique.* PhD thesis, Pierre and Marie Curie University - Paris VI, France, 2008.

[68] M. Chavez-Modena, *Analysis and optimization of multiple-relaxation lattice Boltzmann methods for under-resolved flow simulations.* PhD thesis, Technical University of Madrid, Spain, 2019.

[69] P. Dellar, "Bulk and shear simulations in lattice boltzmann equations," *Phys. Rev. E*, vol. 031203, 2001.

[70] M. Minion and D. Brown, "Performance of under-resolved twodimensional incompressible flow simulations, ii," *Journal of Computational Physics*, vol. 138, pp. 734–765, 1997.

[71] Z. J. Wang, K. Fidkowski, R. Abgrall, F. Bassi, D. Caraeni, A. Cary, H. Deconinck, R. Hartmann, K. Hillewaert, and H. T. H. *et al.*, "High-order cfd methods: current status and perspective," *International Journal for Numerical Methods in Fluids*, vol. 72, pp. 811–845, 2013.

[72] M. Geier, A. Greiner, and J. G. Korvink, "Cascaded digital lattice boltzmann automata for high reynolds number flow.," *Physical Review E*, vol. 73, 2006.